RHEOLOGY AND FLOW OF MUCUS IN HUMAN BRONCHIAL EPITHELIAL CELL CULTURES

Yuan Jin

A dissertation submitted to the faculty at the University of North Carolina at Chapel Hill in partial fulfillment of the requirements for the degree of Doctor of Philosophy in the Department of Mathematics.

Chapel Hill
2015

Approved by:

M. Gregory Forest

Paula Vasquez

David Hill

Jingfang Huang

Laura Miller

ABSTRACT

Yuan Jin: Rheology and Flow of Mucus in Human Bronchial Epithelial Cell Cultures
(Under the direction of M. Gregory Forest)

The propulsion of mucus in human airways toward the trachea by the collective and coordinated action of cilia, known as mucociliary clearance, remains an outstanding modeling and computational challenge. A model system for mucociliary clearance is provided by human bronchial epithelial (HBE) cell cultures that generate macroscopic mean rotational flow. We coarse grain the coordinated cilia propulsion into an imposed dynamic velocity condition on the flat base of a cylinder. A multi-mode Giseskus nonlinear viscoelastic constitutive model derived from rheological data of mucus is employed for the mucus layer. The full system of governing equations for the transient and stationary axisymmetric flow field and air-mucus interface is solved numerically. Our modeling is the first step toward a platform for several purposes: to test accuracy of the constitutive modeling of mucus; to build a faithful model of the cilia-mucus boundary condition; to simulate both the flow and stress fields throughout the mucus layer; to explore the linear and nonlinear viscoelastic behavior of the mucus flow; and to explore the advection-diffusion process of a drug concentration dropped at the surface of the cell culture, and illustrate how the absorption by the bottom plate varies versus the initial drop position and the diffusion coefficient.

ACKNOWLEDGMENTS

I would like to express my deep appreciation and gratitude to my advisor Dr. Forest, for his extraordinary guidance, support and encouragement during my graduate study. I'd also like to thank my entire committee: Paula Vasquez, David Hill, Jingfang Huang and Laura Miller.

I am so thankful for the love and encouragement that my wife Lu had been giving me during the last five years. I am also very grateful for the support of my parents, who have always believed in me and encouraged me to take new challenges.

TABLE OF CONTENTS

LIST OF FIGURES

CHAPTER 1

RHEOLOGY OF MUCUS

1.1 Introduction to Viscoelastic Fluid

For elastic solids, when undergoing deformation, the stress is always proportional to strain (deformation) but independent of the rate of the strain, in accordance with the Hooke's law. For viscous fluids, the stress is proportional to the rate of the strain, but independent of the strain itself, in accordance with the Newton's Law. Viscoelastic materials are intermediate between elastic solids and viscous fluids and may exhibit behaviors which combine liquid-like and solid-like characteristics [7] [15] [18]. Examples of viscoelastic materials may include food, polymers, bio-fluids, as well as the mucus inside human air-way and lung that we will focus on in Chapter 2. One example of viscoelastic behavior is the so-called Weissenberg or rod-climbing effect [5]. When a rod is set to rotate in a Newtonian fluid, the inertial force push the material to the outside of the container. However, for some viscoelastic fluids, stress will develop along the normal axes of the flow field and push the fluids to "climb" up along the rotating rod. The relations between stress, strain and their time dependences of a viscoelastic material are described by the constitutive equations [7] [15] [18]. In this chapter, we illustrate the dynamic modulus for viscoelastic fluid in small amplitude oscillatory shear (SAOS) (Section 1.2). And we review the techniques for modeling nonlinear viscoelastic properties in large amplitude oscillatory shear (LAOS) (Section 1.2). Both the SAOS and LAOS are rheological experiments that are commonly used to probe the viscoelastic properties of complex fluids. We introduce three simple linear constitutive models (Section 1.3) and two nonlinear viscoelastic models (Section 1.3).

1.2 Small Amplitude Oscillatory Shear

When viscoelastic materials are subjected to a small amplitude sinusoidally oscillating strain, the stress is neither exactly in phase with the strain (as it would for a elastic solid), nor 90° out of

phase (as it would for a viscous liquid), but is somewhere in between [15].

In small amplitude oscillatory shear (SAOS) experiment [15], one imposes a sinusoidal strain and measure the resulted stress. The strain is $\gamma = \gamma_0 \sin(\omega t)$, the strain rate is $\dot{\gamma} = \gamma_0 \cos(\omega t)$, and the resulted stress can be decomposed as,

$$\begin{aligned}
\sigma &= G^* \gamma_0 \sin(\omega t + \delta) \\
&= G^* \gamma_0 [\sin(\omega t)\cos(\delta) + \cos(\omega t) sin(\delta)] \\
&= (G^* \cos(\delta)) \cdot \gamma_0 \sin(\omega t) + (G^* \sin(\delta)) \cdot \gamma_0 \cos(\omega t) \\
&= [G^{'} \cdot \sin(\omega t) + G^{''} \cdot \cos(\omega t)]\gamma_0 \\
&= G^{'}\gamma + \frac{G^{''}}{w}\dot{\gamma}
\end{aligned}$$

$G^{'}$ and $G^{"}$ are the storage and loss modulus of the viscoelastic materials. The storage modulus measure the stored energy, representing the elastic portion; and the loss modulus measure energy dissipated as heat, representing the viscous portion.

1.3 Simple Mechanical Models for Viscoelastic Materials

Solid-like behavior is described by Hooke's Law, and represented by a spring [Figure 1.1] mechanical analog.

$$\tau = G\gamma$$

where τ is the stress, G is the elastic modulus of the material, and γ is the strain.

Figure 1.1: "Spring" element of solid-like behavior

Liquid-like behavior is described by Newton's law, and represented by using a dashpot [Figure 1.2] mechanical analog:

$$\tau = \eta\dot{\gamma}$$

where τ is the stress, η is the viscosity of the material, and $\dot{\gamma}$ is the strain rate.

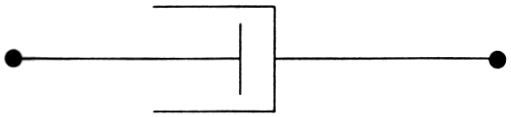

Figure 1.2: "Dashpot" element of liquid-like behavior

Viscoelastic behavior has elastic and viscous components, and can be modeled as linear combinations of springs and dashpots, respectively. Each model differs in the arrangement of these elements.

- *Maxwell model*

  Constitutive equation,

$$\eta\dot{\gamma} = \frac{\eta}{G}\dot{\sigma} + \sigma$$

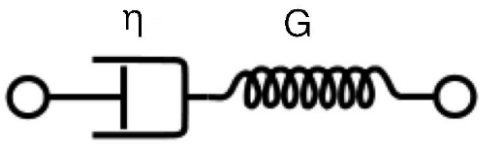

Figure 1.3: Illustration of Maxwell model

- *Kelvin-Voigt model*

  Constitutive equation,

$$\eta\dot{\gamma} + G\gamma = \sigma$$

- *Jeffrey model*

  Constitutive equation,

$$(\eta_1 + \eta_2)\dot{\sigma} + G\sigma = \eta_2 G\dot{\gamma} + \eta_1\eta_2\ddot{\gamma}$$

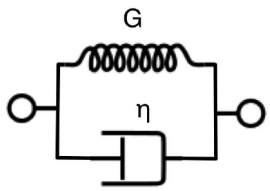

Figure 1.4: Illustration of Kelvin-Voigt model

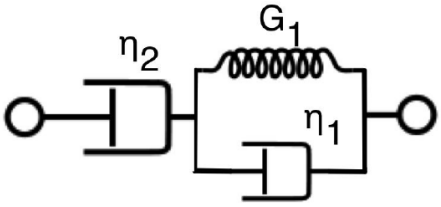

Figure 1.5: Illustration of Jeffrey model

1.3.1 Nonlinear Constitutive Models

- *Giesekus model*

  The Giesekus model [8] is based on the concept of anisotropic drag between the solvent and polymer molecules. The latter is represented by Hookean dumbbells immersed in a Newtonian solvent. The constitutive equation is

$$\lambda \boldsymbol{\tau}_{(1)} + \boldsymbol{\tau} + \frac{\alpha_g \lambda}{\eta_p} \boldsymbol{\tau} \cdot \boldsymbol{\tau} = 2\eta_p \mathbf{D},$$

  where α_g is a so-called mobility parameter; λ is the fluid relaxation time; and $\eta_p = \eta_0 - \eta_s$ is the polymer viscosity, with η_0 the zero shear viscosity. The strain rate tensor is $2\mathbf{D} = (\boldsymbol{\nabla}\mathbf{v})^T + (\boldsymbol{\nabla}\mathbf{v})$, and the upper convected derivative is defined as,

$$(\cdot)_{(1)} = \frac{\partial}{\partial t} - \mathbf{v} \cdot \boldsymbol{\nabla}(\cdot) - (\boldsymbol{\nabla}\mathbf{v})^T \cdot (\cdot) - (\cdot) \cdot (\boldsymbol{\nabla}\mathbf{v}).$$

- *Rolie-Poly model*

  The Rolie-Poly model [17] also arises from molecular theory, where the polymer molecules are modeled as chains that can relax out of their entanglements through reptation, retraction,

convection, and convective constraint release mechanisms. In differential form the model is given by

$$\lambda \boldsymbol{\tau}_{(1)} + \boldsymbol{\tau} + 2\frac{\lambda}{\lambda_R}(1 - f_{tr})\left[(1 + \beta_{RP} f_{tr})\boldsymbol{\tau} + G_0 \mathbf{I}\right] = 2\eta_p \mathbf{D},$$

where

$$f_{tr} = \sqrt{\frac{3}{3 + tr(\boldsymbol{\tau}/G_0)}}.$$

Here the plateau modulus is $G_0 = \eta_0/\lambda$ and the two relaxation times in the model are the reptation time λ and the retraction time λ_R.

1.4 Large Amplitude Oscillatory Shear Analysis

For oscillatory shear experiment, when the strain amplitude is sufficiently large, the material response will become nonlinear and the SAOS modulus $G^{'}$ and $G^{"}$ are no longer sufficient. Because $G^{'}$ and $G^{"}$ in SAOS are based on the assumption that the stress response is purely sinusoidal (linear). However, a nonlinear stress response is not a perfect sinusoid and the viscoelastic modulus are not uniquely defined. Therefore, other techniques are needed for quantifying the nonlinear material response under LAOS deformation [5].

The mathematical structure of the nonlinear stress response is fully captured by the higher Fourier harmonics,

$$\sigma = \gamma_0 \sum_{n:odd} \left\{ G'_n \sin(n\omega t) + G''_n \cos(n\omega t) \right\}$$

The intensity of the higher harmonics could work as a measure of nonlinearity, but these coefficients lack a clear physical interpretation [5].

Another qualitative measure of nonlinear viscoelastic response is the Lissajous curves [22] [5]. Elastic Lissajous curves show the plot of oscillatory stress versus input strain, whereas in viscous Lissajous curves one plots the stress against the rate of strain. For an elastic solid, the elastic Lissajous curves are represented by straight lines and viscous Lissajous curves by circles, while the opposite is true for a viscous fluid. In the small amplitude regime for a generic viscoelastic fluid, both Lissajous curves are ellipses. Departures from an ellipse signal that the nonlinear LAOS regime has been reached.

Cho et al. [4] proposed stress decomposition (SD) into elastic and viscous contributions based

on geometric considerations. They showed that these contributions are one-to-one functions of the strain and the strain rate respectively, so that they become one-dimensional lines in the elastic and viscous Lissajous curves. This overcomes the problem of characterizing two-dimensional ellipses in the Lissajous curves. They proved that for LAOS there exists one unique decomposition(denote $x = \gamma$ and $y = \dot{\gamma}/\omega$)

$$\sigma(x, y) = \sigma^{'}(x, \gamma_0) + \sigma^{''}(y, \gamma_0)$$

where $\sigma^{'}(x)$ and $\sigma^{''}(y)$ represent "elastic" stress and "viscous".

Ewoldt et al. [6] then used Chebyshev polynomials as orthonormal basis functions to further decompose these stresses into harmonic components having physical interpretations.

$$\sigma^{'}(x) = \gamma_0 \sum_{n\ odd} e_n(\omega, \gamma_0) T_n(x)$$

$$\sigma^{''}(y) = \gamma_0 \sum_{n\ odd} v_n(\omega, \gamma_0) T_n(y)$$

They developed several nonlinear metrics for LAOS using the Chebyshev coefficient above. These metrics also have a direct geometrical representation in the Lissajous curves, and have the advantage of not being based on individual harmonic contributions.For example, $e_3 > 0$ indicates strain-stiffening, $e_3 < 0$ indicates strain-softening, $v_3 > 0$ indicates shear-thickening, and $v_3 < 0$ indicates shear thinning.

CHAPTER 2

MODELING OF MUCUS FLOW IN HBE CELL CULTURE

2.1 Introduction

The propulsion of mucus in human airways to the trachea by the collective, coordinated action of cilia, known as mucociliary clearance, remains an outstanding modeling and computational challenge. A predictive model has medical relevance since failure to clear mucus from the airways leads to chronic, even fatal, lung infections. Additionally, the causal relationship between mucus rheology and mucociliary clearance remains an open problem in the field. The three major modeling components of mucociliary clearance are: a constitutive model for mucus based on rheological data, a mechanism (forcing condition) for mucus propulsion either by individual cilia or carpets of cilia, and numerical methods to solve the full system of equations [25]. Validation of each component in airway simulations is essentially impossible due to the lack of in vivo experimental data and resolution of airway mucus transport.

A transformative model system for the study of mucociliary clearance is provided by human bronchial epithelial (HBE) cell cultures, whereby an epithelial tissue, a layer of fluid surrounding the cilia, and an overlying mucus layer, are grown in a cylindrical dish [Figure 2.2] [9]. These cell cultures generate macroscopic mean flow in a clockwise or counterclockwise motion, forming what appears from above as a rotating vortex or mucus hurricane [Figure 2.4].

Our goal here is to simulate the flow of mucus in a HBE cell culture, both as a first modeling step to aid experimental studies, and as a constitutive model test for mucus against cell culture observations. We employ a multi-mode Giesekus nonlinear viscoelastic constitutive law for the mucus layer. The Giesekus model is a canonical nonlinear constitutive model that captures shear thinning and first and second normal stress generation in shear [8]. In this chapter, multiple modes are used to approximate the broad relaxation spectrum of mucus. We coarse grain the cilia propulsion mechanism into an imposed dynamic velocity condition on the flat base of a cylinder. In addition,

the air-mucus interface is treated as a free boundary, whose shape is investigated with the effect of surface tension. We develop a numerical algorithm and implement it to solve the full system of governing equations for the transient and stationary axisymmetric flow field and air-mucus interface, and explore the mass transport of mucus as a function of the Giesekus constitutive properties and the imposed driving condition at the lower plate. We studied the nonlinear viscoelastic properties of our multi-mode Giesekus constitutive model in the cell culture. And we explore the advection-diffusion process of a drug concentration dropped at the surface of the cell culture.

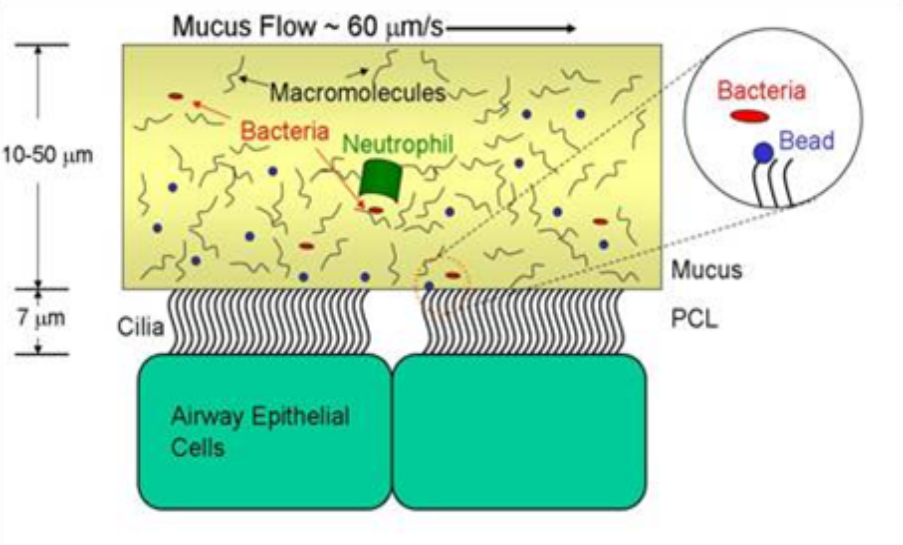

Figure 2.1: Mucociliary clearance in human airway (David Hill)

2.1.1 HBE Cell Cultures

The primary human bronchial epithelial (HBE) airway cell culture is an invaluable model system of the human airway. These cultures, developed by Lencher and coworkers [16], grow to confluence with cell differentiation into goblet cells that produce mucin proteins and ciliated cells that sprout active cilia, forming epithelial tissue that draws nutrients and water from the reservoir below the membrane. Within weeks, an air-mucus interface forms over a mucus layer of $\sim 10-50$ microns, with a periciliary liquid layer (PCL) between mucus and tissue approximately 7 microns thick. Ciliated cells (~ 200 per ciliated cell, each ~ 8 microns long at full extension of the power stroke) coordinate their individual power-return stroke with $\sim\ 10-15Hz$ frequency, propelling the mucus layer in the culture either clockwise or counterclockwise. From above, the flow pattern resembles a hurricane,

and thus the expression mucus hurricanes was born [Figure 2.4A]. Once coordinated transport of the mucus layer is established, fluorescent tracer particles [19], [2], gold nanorods [21], or endogenous cellular debris [21], [3] can be tracked to gain flow profile information. For cultures whose cilia synchronize and transport mucus around the dish, a true ex vivo model assay is provided for a detailed study of a wide range of pulmonary physiology. Cells are obtained from donors of various disease populations including Chronic Obstructive Pulmonary Disease (COPD) and Cystic Fibrosis, reproducing acquired and genetic mutations, thereby serving as a model for disease pathology and as a testbed for flow and rheological consequences of drug or physical therapies.

Figure 2.2 shows a picture of one HBE cell culture from David Hill's lab. Figure 2.3 illustrates the detailed dimensions of the HBE cell culture. The radius of the cell culture is around $13.3mm$. The height of cell culture is around $12.3mm$, and the depth of the mucus layer in HBE cell cultures ranges from $10 - 50\mu m$ [11]. Therefore, we have a relatively large aspect-ratio of the cell culture radius over the depth of the mucus layer, which ranges from $1000 - 50$.

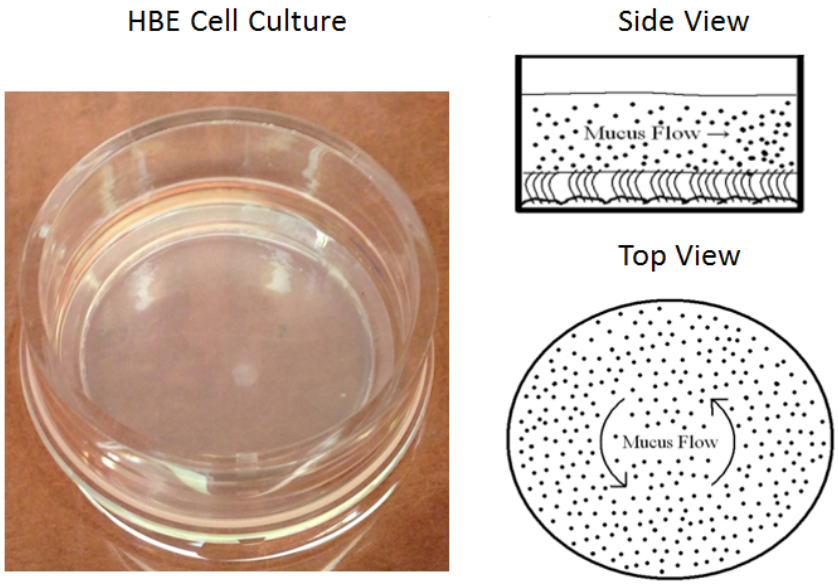

Figure 2.2: Schematic of an HBE Cell Culture

In this work, experimental data from micro and macrorheology are used to construct a nonlinear constitutive model of mucus. We refer to recent studies of biochemical composition [14] [9] [11] properties of sputum, and cell culture mucus. For this initial study, we avoid the open question

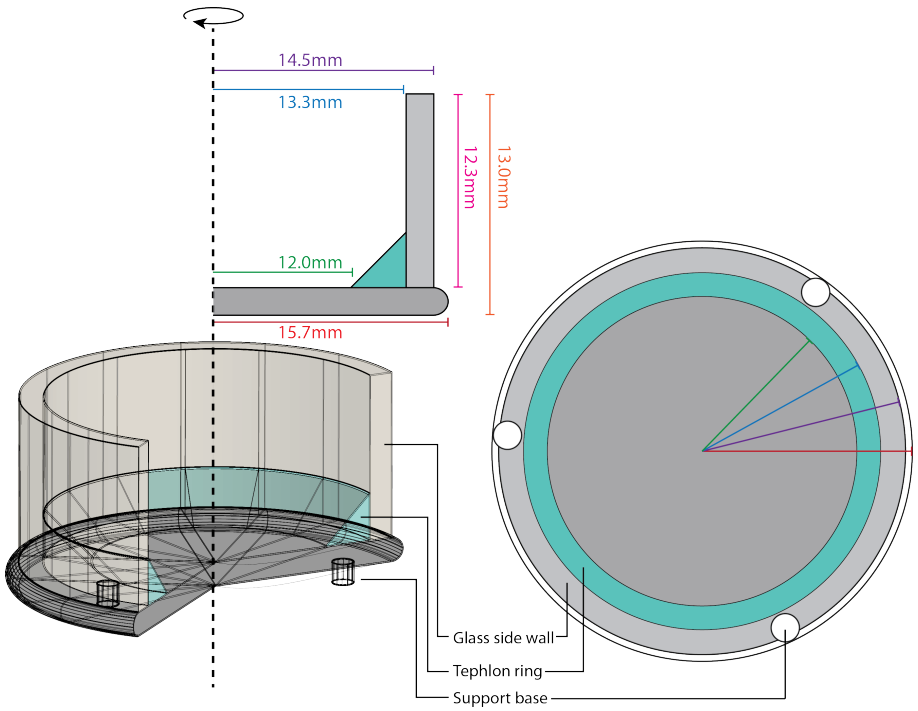

Figure 2.3: HBE Cell Culture Geometry (John Melnick)

of cilia-mucus propulsion, and idealize the forcing mechanism of the power and return stroke as though the cilia were uniformly synchronized. The actual momentum transfer mechanism between the PCL and mucus layers remains one of the most important unsolved problems in lung mechanics. We do not address this problem in the current paper, since to do so would require detailed modeling of fully three-dimensional fluid flow, single and coordinated nonlinear viscoelastic fluid-structure interactions, and a heterogeneous, dynamic, cilia-PCL-mucus boundary condition. Instead, we coarse grain the PCL as a moving solid boundary, averaging out the scales of the coordinated cilia to study the mean mucus transport features due to a homogeneous dynamic cilia carpet consisting of a power stroke and a return stroke.

2.1.2 Mucus Flow in HBE Cell Cultures

Due to the cylindrical geometry of the culture wares used in the growth of HBE cultures, mucus transport in these system is rotational, forming so-called mucus "hurricanes" [Figure 2.4A] [19] that serve as the basis of the modeling of mucociliary transport presented herein. Experiments reveal a rotational velocity of the mucus layer that is approximately linear in the radial distance from the

center as shown in Figure 2.4B.

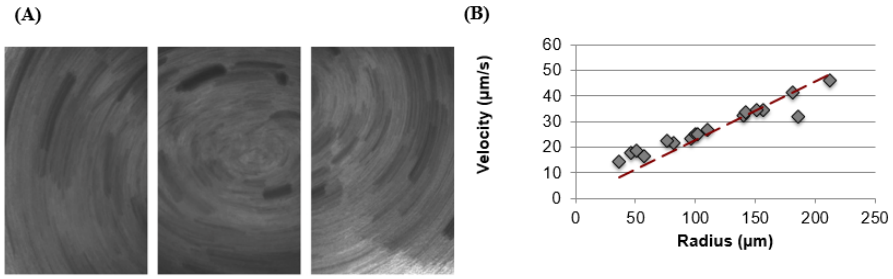

Figure 2.4: Demonstration of rotational mucus transport in HBE cell cultures. (A) Traces of 1 mm fluorescent micro-spheres at the culture surface from a 5 second time lapse exposure. (B) Linear velocities of the particles versus distance from the center of rotation. Data extrapolated from [21]. With the rotational flow, the mucus tend to swell up in the middle of the HBE cell culture, forming a dome shape for the free surface of the mucus flow, see Figure 2.5.

Also note here that though the cilia carpet and mucus layer cover the whole cell culture, the observed mucus "hurricane" only forms at the middle part of the cell culture, which makes the radius of the mucus "hurricane" less than $13.3mm$ and could be as low as around $4mm$.

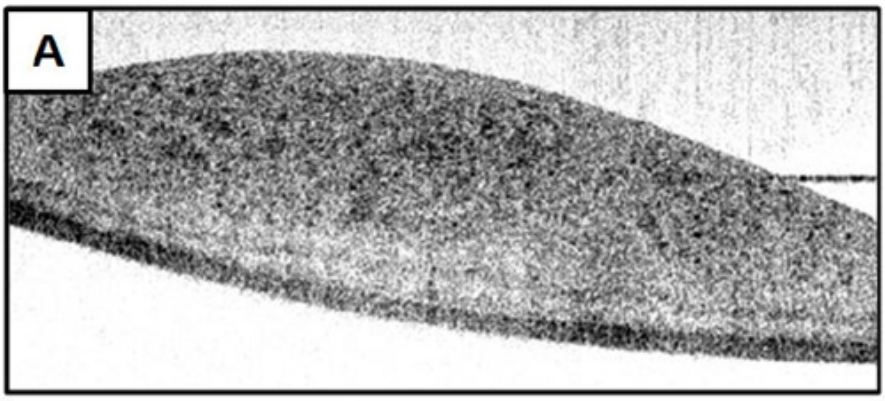

Figure 2.5: Surface shape of an HBE cell culture shows the dome at the center [21]

2.1.3 Axisymmetric Assumption

As noted above, for this study we suppress heterogeneity of the cilia forcing condition, tantamount to a two-dimensional long-wave limit of the ciliary metachronal wave. The ciliated carpet is thereby replaced by a flat rigid disc that moves with a prescribed, non-monotonic, angular velocity that

mimics the power and return strokes of cilia. This coarse-graining of the cilia carpet is self-consistent with axisymmetry of the three flow variables, pressure, and free surface, affording a reduction in the computation from three to two space dimensions, as shown in Figure 2.6.

With the axisymmetric assumption, the computational domain consists of a cylinder of radius R and height Z, and a layer of viscoelastic fluid of initial uniform height H. The fluid is set into motion by a rotating disk at the bottom of the cylinder with an imposed angular velocity, ω, which we vary to mimic forward and return strokes of cilia. By axisymmetry, each scalar variable depends only on (r, z); therefore, the computational domain is a 2D rectangle $[0, R] \times [0, Z]$ [Figure 2.6 left]. The air-liquid interface is free, with surface tension estimated from the literature [13], as explained below.

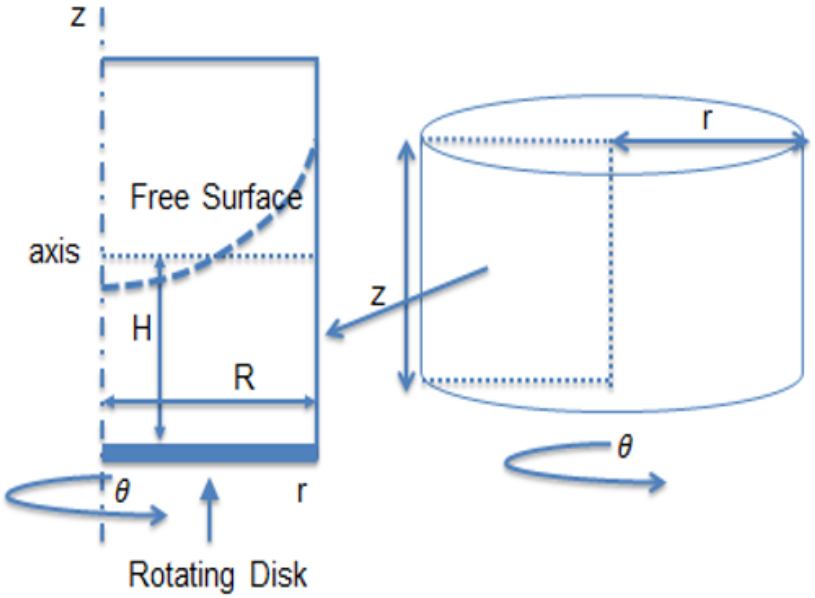

Figure 2.6: HBE cell culture in cylindrical coordinates and reduction from 3D cylinder to 2D rectangular region based on the axisymmetric assumption

2.2 Model Equations

For an incompressible, isothermal, non-Newtonian fluid, the conservation of mass and momentum equations are,

$$\nabla \cdot u = 0$$

$$\rho(\frac{\partial \boldsymbol{u}}{\partial t} + \boldsymbol{u} \cdot \nabla \boldsymbol{u}) = -\nabla p + \eta_s \Delta \boldsymbol{u} + \nabla \cdot \boldsymbol{\tau} + \rho \boldsymbol{g}$$

where ρ is the fluid density and η_s is the solvent viscosity. To close the system, a constitutive equation for the extra stress tensor $\boldsymbol{\tau}$ is needed. We use both linear and nonlinear viscoelastic data from cell culture mucus to construct the constitutive model, as explained in Section 2.3. We assume a multi-mode nonlinear viscoelastic model,

$$\boldsymbol{\tau} = \sum \boldsymbol{\tau_i}$$

where each mode is governed by a constitutive equation of the so-called Giesekus form,

$$\boldsymbol{\tau_i} + \lambda_i \boldsymbol{\tau_{i(1)}} + \frac{\alpha \lambda_i}{\eta_{p,i}} \boldsymbol{\tau_i} \cdot \boldsymbol{\tau_i} = \eta_{p,i} \dot{\gamma}$$

here, for each mode, λ_i is a relaxation time and $\eta_{p,i}$ is the polymer contribution to the viscosity. The total viscosity, η_0, is the sum of the solvent and mode contributions, $\eta_0 = \eta_s + \sum \eta_{p,i}$. In addition, $\dot{\gamma} = (\nabla \boldsymbol{u} + \nabla \boldsymbol{u^T})$is the rate of strain tensor, and the subscript notation $\boldsymbol{\tau}_{(1)}$ denotes the upper convected derivative (that guarantees the model is invariant under rigid body motions or coordinate changes), given by

$$\boldsymbol{\tau_{(1)}} = \frac{\partial \boldsymbol{\tau}}{\partial t} + \boldsymbol{u} \cdot \nabla \boldsymbol{\tau} - \boldsymbol{\tau} \cdot \nabla \boldsymbol{u} - \nabla \boldsymbol{u^T} \cdot \boldsymbol{\tau}$$

In the Giesekus model, α is the tunable nonlinearity parameter, called the mobility parameter; in the limit $\alpha = 0$, the Giesekus model reduces to the Upper Convected Maxwell (UCM) model. The UCM model captures the fundamental viscoelastic property of normal stress generation in shear flows, whereas the quadratic nonlinearity of the mobility term in the Giesekus model is necessary to capture shear thinning.

2.2.1 Nondimensionalizaion

The characteristic scales are chosen as follows. Time is scaled by the rotation frequency of the lower plate, ω, the fluid velocity is scaled by the angular velocity of the outer edge of the disk, ωR, the characteristic stress is taken to be a total viscous stress $\omega\eta_0$, and the characteristic pressure is chosen as $\rho\omega^2R^2$, so that the dimensionless time, velocity, stress, and pressure (denoted by prime superscripts) become

$$t' = t\omega,\ u' = \frac{u}{\omega R},\ \tau' = \frac{\tau}{\eta_0\omega},\ P' = \frac{P}{\rho\omega^2R^2},\ r' = \frac{r}{R},\ z' = \frac{z}{R}$$

The key dimensionless groups are identified as the Reynolds number Re, Weissenberg number We (normalized elastic relaxation time), the ratio of solvent viscosity to total viscosity β_s, and the Froude number Fr (inertia relative to gravity):

$$Re = \frac{\rho\omega R^2}{\eta_0},\ We = \lambda_L\omega,\ \beta_s = \frac{\eta_s}{\eta_0},\ Fr = \frac{\omega^2 R}{g}$$

where λ_L is chosen as the longest elastic relaxation time within the multimode Giesekus model. Dropping the prime superscript, the non-dimensional governing and constitutive equations are

$$\nabla \cdot u = 0$$

$$\frac{\partial \boldsymbol{u}}{\partial t} + \boldsymbol{u}\cdot\nabla\boldsymbol{u} = -\nabla p + \frac{\beta_s}{Re}\Delta\boldsymbol{u} + \frac{1}{Re}\nabla\cdot\boldsymbol{\tau} + \frac{1}{Fr}\hat{\boldsymbol{e_Z}}$$

$$\boldsymbol{\tau_i} + We\tilde{\lambda_i}\boldsymbol{\tau_{i(1)}} + \frac{We\tilde{\lambda_i}}{\beta_i}\alpha(\boldsymbol{\tau_i}\cdot\boldsymbol{\tau_i}) = \beta_i\dot{\boldsymbol{\gamma}}$$

where $\tilde{\lambda_i} = \lambda_i/\lambda_L$, $\beta_i = \eta_{p,i}/\eta_0$ and $\hat{\boldsymbol{e}_z}$ is the unit vector in the z-direction.

2.3 Data-derived Nonlinear Constitutive Model

To select the modeling parameters for the multi-mode Giesekus model, our approach is to use experimental data to identify linear (small amplitude) storage and loss moduli across a physiological frequency range, and then to use a discrete set of UCM modes ($\alpha = 0$) that gives a fit to the experimental data. We use data generated from a fixed-strain frequency sweep in a cone and plate

TA Instruments AR-G2 rheometer and a 2.5$wt\%$ HBE mucus sample, representative of the healthy range of human lung mucus. The data and corresponding fit using five UCM modes is shown in Figure 2.7(A), with the parameter results shown in Table 2.3.

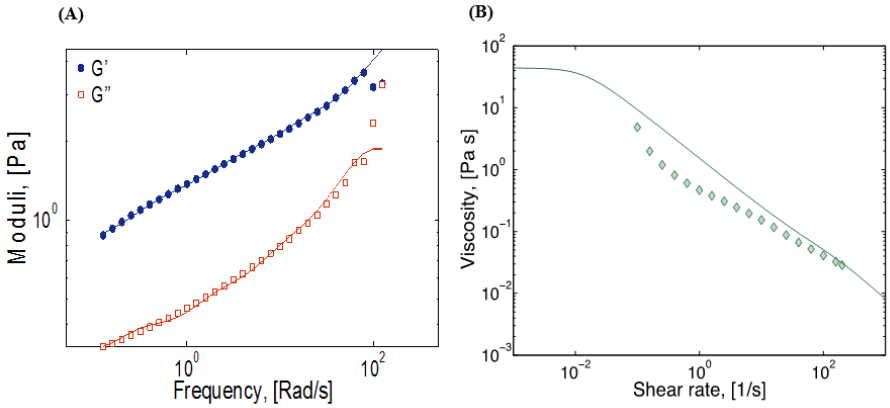

Figure 2.7: (A) Linear dynamic storage (G) and loss (G) moduli data (solid, open dots) for 2.5$wt\%$ HBE mucus across a frequency range, together with the corresponding fit to 5 UCM modes. (B) Viscosity vs. shear rate data for 2.5$wt\%$ HBE mucus and corresponding fit to a sum of 5 Giesekus modes. The curve shown is the best fit under the condition $0\alpha 0.5$. Model parameters are given in Table 1. Data courtesy of Jeremy Cribb and David Hill.

The shear thinning of mucus is captured by the mobility parameter , which we restrict to the range $0 \leq \alpha \leq 0.5$, since values greater than 0.5 result in non-monotonic flow curves. To find the best fit for the nonlinear mobility parameters per Giesekus mode, we use rheometric data of the shear-thinning flow curve (the viscosity versus shear rate), as shown in Figure 2.7(B).

Mode	Relaxation time [s]	Modulus [Pa]	Giesekus parameter α
1	0.0089	3.3472	0.2
2	0.0821	0.7551	0.3
3	0.4660	0.5350	0.5
4	3.1290	0.4543	0.5
5	49.733(λ_L)	0.8486	0.5

2.4 Coarse-graining of the Cilia Carpet Driving Conditions

The beating of a single cilia is periodic and asymmetric, as illustrated in Figure 2.8, which consists two phases : a forward power stroke (or effective stroke) in which the tips of the fully extended cilia

penetrate the mucus layer, and a return stroke (or recovery stroke) in which the cilia do not engage the mucus layer but still induce some mild backflow. All the cilia that forms the cilia carpet at the bottom of the cell culture beat in a coordinated fashion, create metachronal wave and propel the mucus to rotate in the cell culture. The rotational movement of the mucus induced by the cilia carpet is also periodic and asymmetric. According to our experimental observation, because of the cilia forcing condition at the bottom, mucus moves in the angular direction about $10\mu m$ in one forward cycle of $0.1s$ and then moves about $5\mu m$ in one backward cycle of $0.1s$ near the edge of the cell culture.

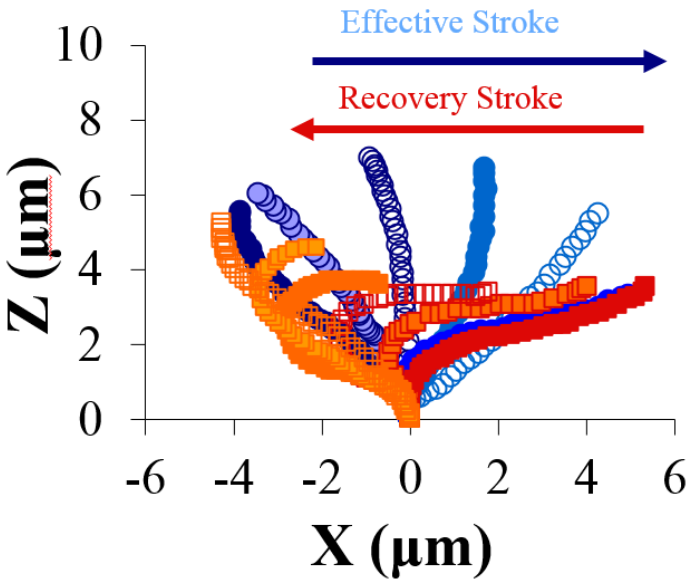

Figure 2.8: Movement of a single cilium: power stroke and recovery stroke. Data replotted from [23] and adapted from [10].

We coarse grain the cilia propulsion mechanism into an imposed dynamic velocity condition $u_\theta \mid_{z=0}$ on the flat base of a cylinder. As mentioned in Section 2.1.2, the rotational velocity of the mucus "hurricane" is approximately linear in the radial distance from the center. Therefore, as a first step, we model the cilia driving condition with an angular velocity ω, where $u_\theta \mid_{z=0} = \omega r$

If we use a simple constant angular velocity $\omega = \omega_0$, resulting profile is the so-called swirling flow. This does not match the periodic and asymmetric driving force of the cilia carpet. However, swirling flow provide us a simple case where we can benchmark our numerical method, as well as compare the difference between Newtonian fluid and our nonlinear viscoelastic fluid.

In order to simulate the two phases of cilia driving condition, we use a periodic angular velocity with potential to change directions, $\omega = f(t)$, and $f(t)$ is a piece-wise sinusoidal function, given by

$$f(t) = \begin{cases} P_0 \sin(\omega_p t), \ for\ 0 < t < \frac{\pi}{\omega_p} \\ R_0 \sin(\omega_r t), \ for\ 0 < t < \frac{\pi}{\omega_p} + \frac{\pi}{\omega_r} \end{cases}$$

where P_0 and R_0 are the largest angular velocity amplitudes during the power and recovery strokes, and ω_p and ω_r are the frequencies of the power and recovery strokes.

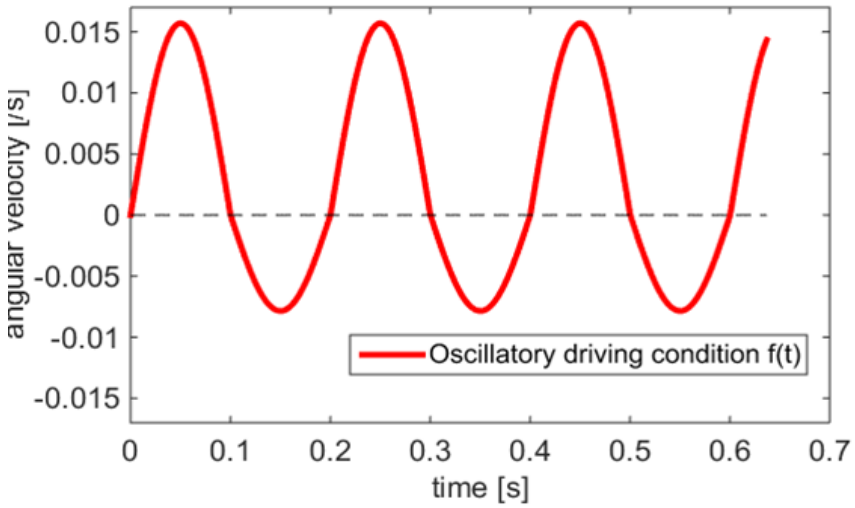

Figure 2.9: The oscillatory driving condition f(t) imposed at the bottom plate to mimic cilia power and return strokes and match experimental observation

We could select a typical set of P_0, R_0, ω_p and ω_r based on our experimental observation,

$$\frac{\pi}{\omega_p} = 0.1, \ \frac{pi}{\omega_r} = 0.1$$

$$\int_0^{0.1} P_0 \sin(\omega_p t) dt = 1 \times 10^{(-5)}, \ \int_0^{0.1} R_0 \sin(\omega_r t) dt = 5 \times 10^{(-6)}$$

Therefore we have $P_0 = 1.57 \times 10^{-2} s^{-1}$, $R_0 = 7.9 \times 10^{-3} s^{-1}$, $\omega_p = 10\pi Hz$ and $\omega_p = 10\pi Hz$.This driving condition is shown in Figure 2.9. Those parameter values are chosen to match some of our experiment observations, therefore they are a reasonable set of parameters for mucus flow the HBE cell culture. For real mucus "hurricane" in HBE cell culture, depend on the different radius of the

"hurricanes" and different observed rotational velocities, the corresponding parameters of P_0 and R_0 could be as high as four times of the above P_0 and R_0.

Note here that $u_\theta \mid_{z=0}$ is a sinusoidal function in time and a linear function in r. Below in Section 2.7, where we wish to apply large amplitude oscillatory shear analysis, we would imposed a sinusoidal shear strain(refer to Section 1.4) rather than a sinusoidal u_θ. In that case, we would have a different type of driving for $u_\theta \mid_{z=0}$(discussed in detail in Section 2.7).

2.5 Numerical Methods

No-slip flow boundary conditions are imposed at the solid walls of the cylinder, bottom and right edges of the rectangle in Figure 2.6. Along the central axis of the cylinder, $r = 0$, we impose a vanishing Neumann condition in the radial coordinate on all flow variables.

Driving conditions at the bottom plate is discussed in Section 2.4. At the bottom corner of the cell culture, we use a boundary layer adjustment for the driving velocity, given by,

$$u_\theta \mid_{z=0}{}^{adjusted} = u_\theta \mid_{z=0} *(1 - e^{\frac{(r^2-R^2)}{\epsilon}})$$

where ϵ is a small number close to zero. This numerical boundary layer adjustment is also consistent with experimental observation that mucus "hurricane" only exist at the middle of the cell culture.

The air-mucus interface is a free moving surface. The surface tension of the air-mucus interface is in the range of $30 - 34mN/m$ [13]. The boundary condition at this free surface is stress balance boundary condition. The effect of the surface tension is incorporated into the stress balance condition through capillary pressure:

$$\hat{\boldsymbol{n}} \cdot \boldsymbol{T} \cdot \hat{\boldsymbol{n}} = P_{cap}$$

$$\hat{\boldsymbol{n}} \cdot \boldsymbol{T} \cdot \hat{\boldsymbol{t}} = 0$$

$$P_{cap} = \sigma\kappa$$

where $\hat{\boldsymbol{n}}$ and $\hat{\boldsymbol{t}}$ are the local unit normal and tangential vectors,$\boldsymbol{T} = -p\boldsymbol{I} + \boldsymbol{\tau}$, is the total stress tensor, P_{cap} is the capillary pressure, σ is the surface tension, and κ is the curvature.

Finite difference method is used with a staggered grid. For the Navier-Stokes part of the fluid

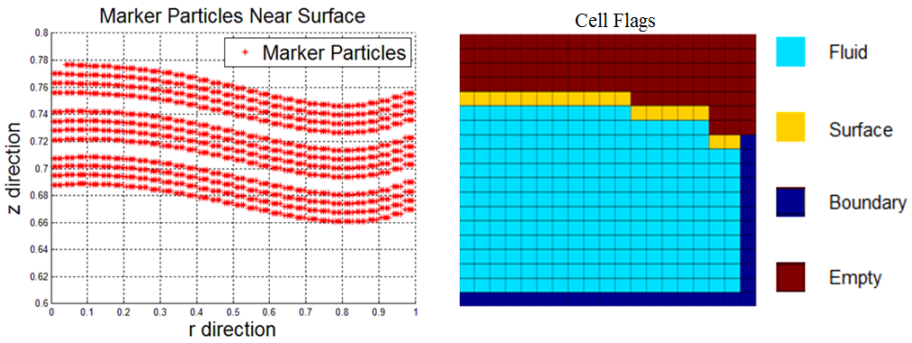

Figure 2.10: Marker and Cell method illustration

equations, we use projection method [1]. Marker and Cell (MAC) method [20] is used here to track the movement of the free surface. In the MAC method, artificial massless trackers are placed near the free surface and are transported according to the fluid velocity. Cells are flagged as fluid cells, surface cells and empty cells based on the location of all markers [Figure 2.10]. Those markers are able to track the free surface movement.

At each time step, the numerical method [24] runs as following:

Step 1, Calculate an arbitrary pressure field $\tilde{P}(r, z, t_0)$ at the free surface that satisfies the free surface boundary condition at $t = t_0$

Step 2, Projection method for Navier-Stokes part of the model equation: first calculate an intermediate velocity field $\tilde{\boldsymbol{u}}(r, z, t)$ using the finite difference form of the momentum equation with correct boundary conditions, with

$$\boldsymbol{u}(r, z, t) = \tilde{\boldsymbol{u}}(r, z, t) - \nabla\varphi(r, z, t)$$

$$\nabla^2\varphi(r, z, t) = \nabla \cdot \tilde{\boldsymbol{u}}(r, z, t)$$

$$P(r, z, t) = \tilde{P}(r, z, t_0) + \varphi(r, z, t)/dt$$

solve the above Poisson equation; then compute the velocity field and update the pressure

Step 3, Integrate the stress constitutive equations using finite difference method and forward Euler time integration

Step 4, Update the locations of marker particles and re-flag all the cells.

$$\frac{dr}{dt} = u_r, \ \frac{dz}{dt} = u_z$$

Step 5, Calculate the shape of the free surface; then find the curvature and surface tension.

2.6 Results

2.6.1 Swirling Flow: Compare Newtonian Fluid with Viscoelastic Fluid

This study of swirling flow is chosen to benchmark the algorithm and to compare the behavior of Newtonian and viscoelastic fluids, prior to a study of HBE cell cultures. We examine the swirling flow of 4 different types of fluids: viscous, viscoelastic with a single UCM mode, viscoelastic with a single Giesekus mode, and multi-mode Giesekus with 5 modes given in Table 2.3.

The parameters used in the following numerical simulations are: cell culture radius $R = 1\times10^{-2}m$, height $Z = 1 \times 10^{-4}m$, initial depth of mucus $H = 5 \times 10^{-5}m$, solvent viscosity $\eta_s = 1mPa \cdot s$, surface tension $\sigma = 3 \times 10^{-2}N/m$.

For the single mode UCM and Giesekus models, we use polymer viscosity $\eta_p = 10Pa \cdot s$, and relaxation time $\lambda = 10s$. In addition, the rotational driving velocity $u_\theta \mid_{z=0}$, of the cilia carpet at the bottom of the HBE cell culture has a constant angular velocity (swirling flow) $\omega = \omega_0$. We use $\omega_0 = 1.57 \times 10^{-2}s^{-1}$, the same as the largest angular velocity of the oscillatory driving condition in Section 2.4.

In Figure 2.11, we show the development of secondary flow patterns at various times at the beginning stages of the swirling flow for Newtonian fluid. Here secondary flow refers to the (u_r, u_z) components of the velocity field, since u_θ is the primary velocity component for a rotational flow. At early times, an outward centrifugal force causes the fluid near the rotating disk to flow radially outward, up the sidewalls of the cylinder, inward along the top, and finally down near the center. A vortex is formed here. After a certain amount of time, the flow will reach a quasi-steady state.

The same type of flow is shown for viscoelastic fluids in Figure 2.12, Figure 2.13 and Figure 2.14. At early times, the secondary flow pattern and vortex is similar to those in Newtonian case. However, as time evolves, this apparently stationary structure destabilizes, breaks up, and forms a new vortex

with opposite orientation. This reverse orientation in the secondary flow is a classical consequence of the generation of normal stresses in viscoelastic fluids; a property shared in all our viscoelastic models. In the quasi-steady state of viscoelastic fluids, the fluid near the rotating disk flows radially inward, up the center of the cylinder, inward along the top, and finally down near the sidewalls. In stark contrast, for Newtonian fluids, the flow near the center is downward while upward near the wall (Figure 2.16). This phenomenon has been long recognized in swirling cylindrical flow, called the so-called Quelleffeck [5], an analog of the Weissenberg effect of rod climbing [5].

The mass flux rate across the $\theta = 0$ plane for all the studied fluids is shown in Figure 2.17. For Newtonian fluids the mass flux is increasing during the transients and eventually reaches a plateau in steady state. However, for single-mode Giesekus and UCM model fluids, in the early transient the mass flux rate first increases similar to the Newtonian flow, then decreases monotonically while converging to steady state. The maximum mass flux rate arises during the formation of the reverse vortex at the bottom corner of the cell culture. For the 5-mode Giesekus model, the transient mass flux rate is non-monotone reflecting the effects of having more than one relaxation modes. Since each fluid model has finite memory, the stationary mass transport rates are identical, irrespective of the differences in secondary flow patterns. Thus there is no enhancement of mass transport for unidirectional swirling flow due to viscoelasticity at steady state.

2.6.2 Numerical Mucus Flow in Cell Culture

In this section, we conduct the numerical simulation for the mucus flow in HBE cell culture. We use the 5-modes Giesekus model from Section 2.3 as our constitutive model for mucus. And the cilia driving condition is modeled as a piece-wise sinusoidal angular velocity function $f(t)$ at the bottom plate given by

$$f(t) = \begin{cases} P_0 \sin(\omega_p t), \ for\ 0 < t < \frac{\pi}{\omega_p} \\ R_0 \sin(\omega_r t), \ for\ 0 < t < \frac{\pi}{\omega_p} + \frac{\pi}{\omega_r} \end{cases}$$

where $P_0 = 1.57 \times 10^{-2} s^{-1}$, $R_0 = 7.9 \times 10^{-3} s^{-1}$, $\omega_p = 10\pi Hz$ and $\omega_p = 10\pi Hz$[Section 2.4].

We first examine the secondary flow profiles in Figure 2.18. As before, the early transient matches the viscous fluid structure, which then destabilizes and reverses orientation of the vortex,

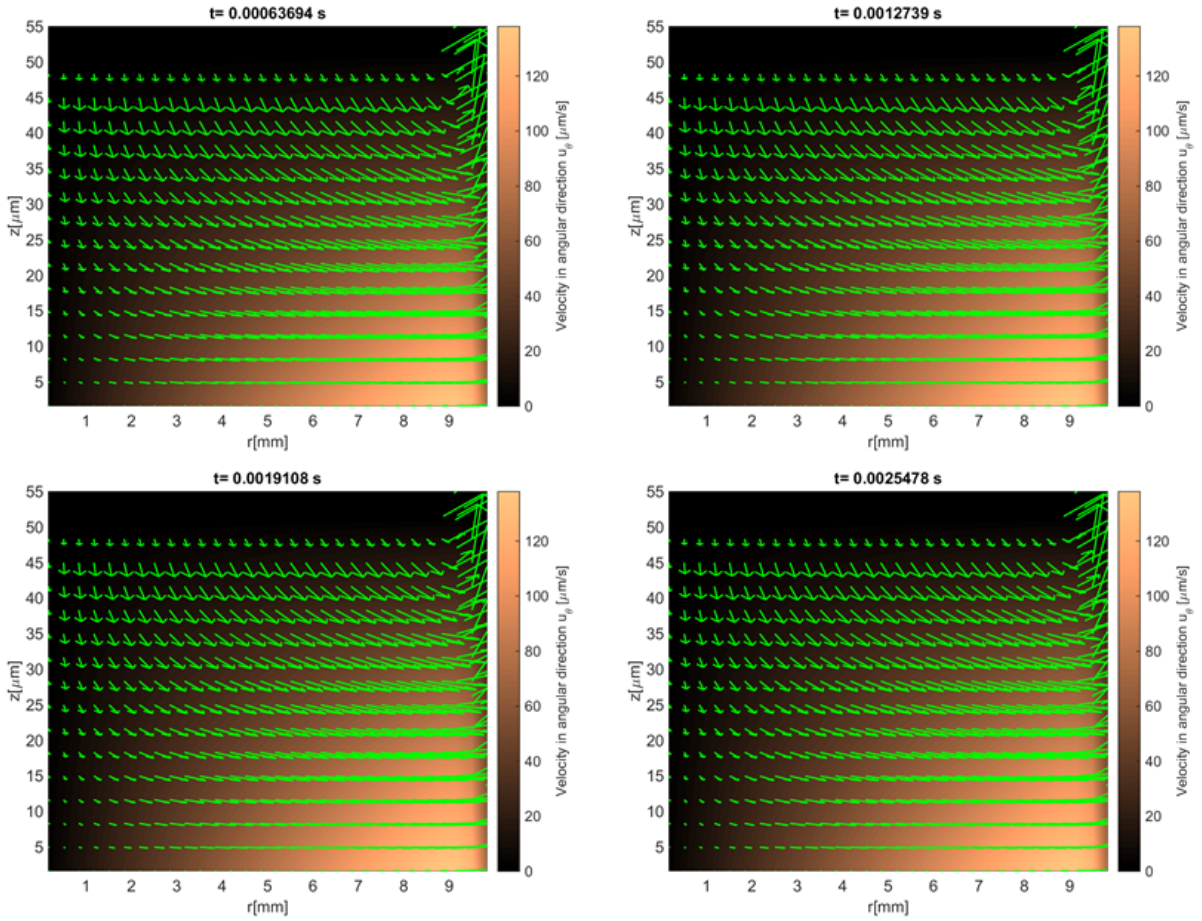

Figure 2.11: Transient process of the flow field for a Newtonian fluid; the velocity field in the plot is the secondary flow (u_r *vs* u_z) and the color map in the background is the primary flow u_θ

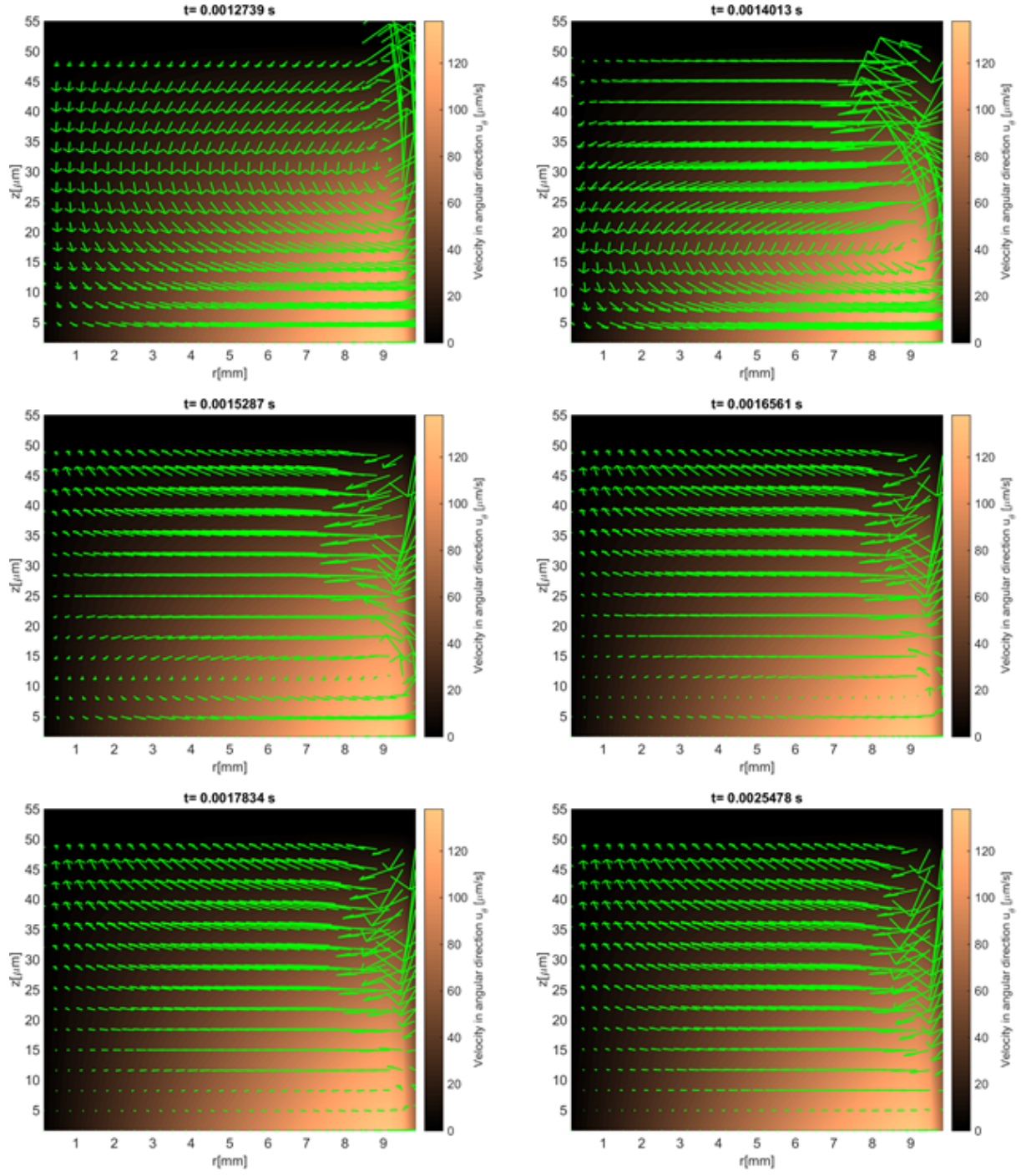

Figure 2.12: Transient process of the flow field for a a single mode UCM fluid; the velocity field in the plot is the secondary flow (u_r vs u_z) and the color map in the background is the primary flow u_θ

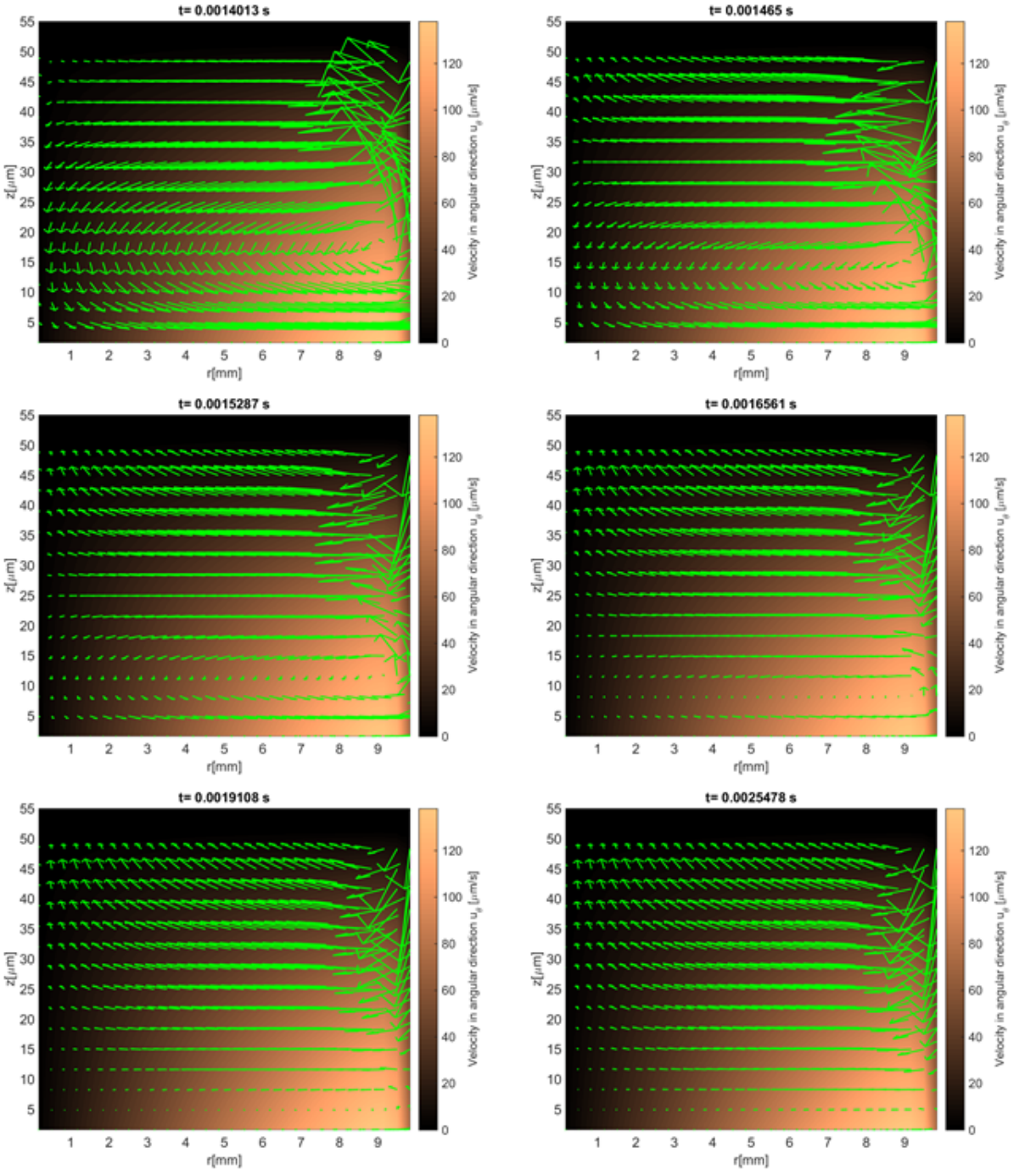

Figure 2.13: Transient process of the flow field for a single mode Giesekus fluid with $\alpha = 0.3$; the velocity field in the plot is the secondary flow (u_r vs u_z) and the color map in the background is the primary flow u_θ

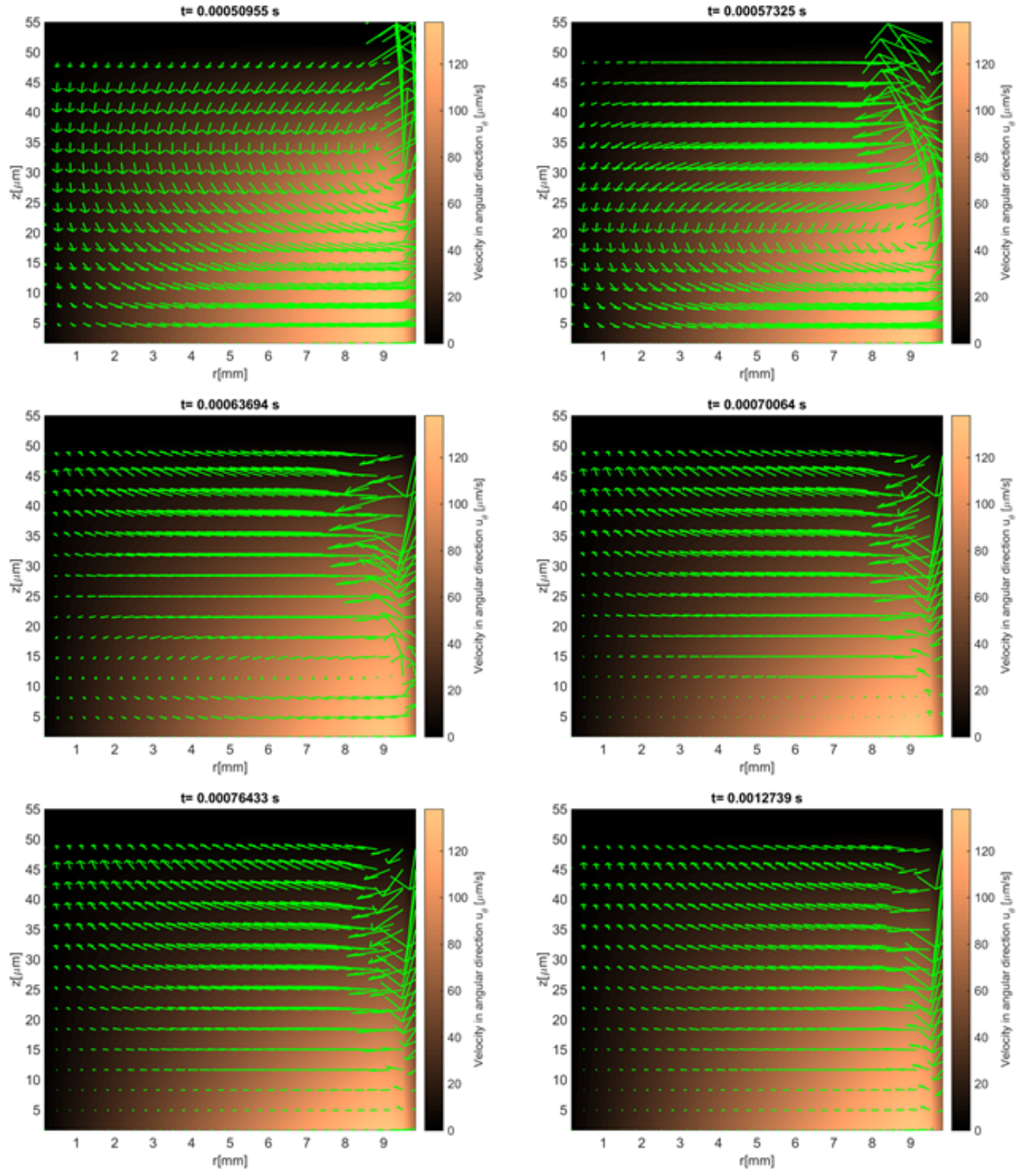

Figure 2.14: Transient process of the flow field for a 5 modes Giesekus fluid with parameters specified in Table 2.3; the velocity field in the plot is the secondary flow (u_r vs u_z) and the color map in the background is the primary flow u_θ

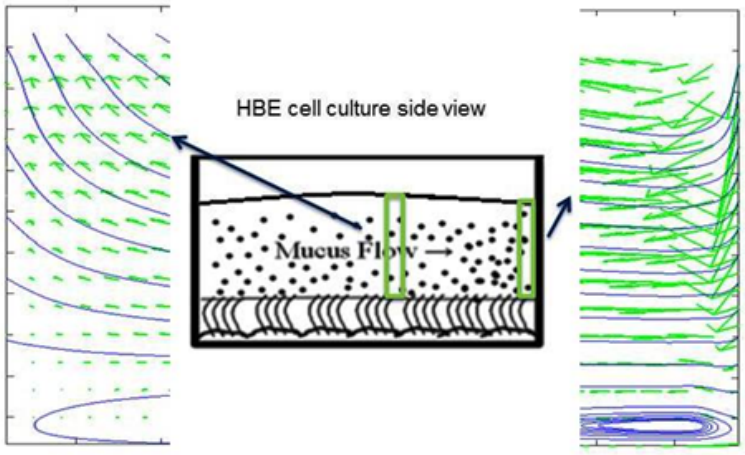

Figure 2.15: The stationary secondary flow field and streamlines for nonlinear viscoelastic mucus model in the middle of the cell culture (left) and at the edge of the cell culture (right).

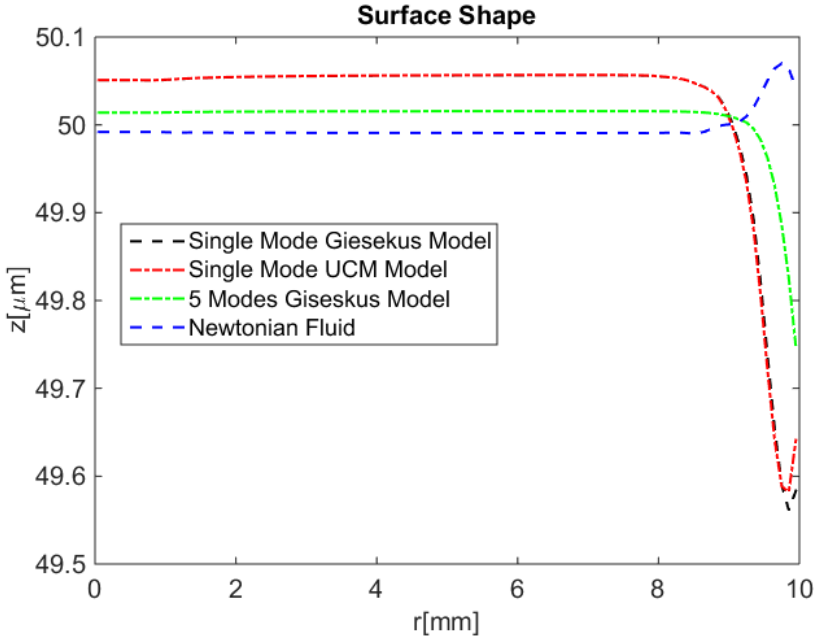

Figure 2.16: Free surface shape at steady state for the swirling flow with different types of fluids

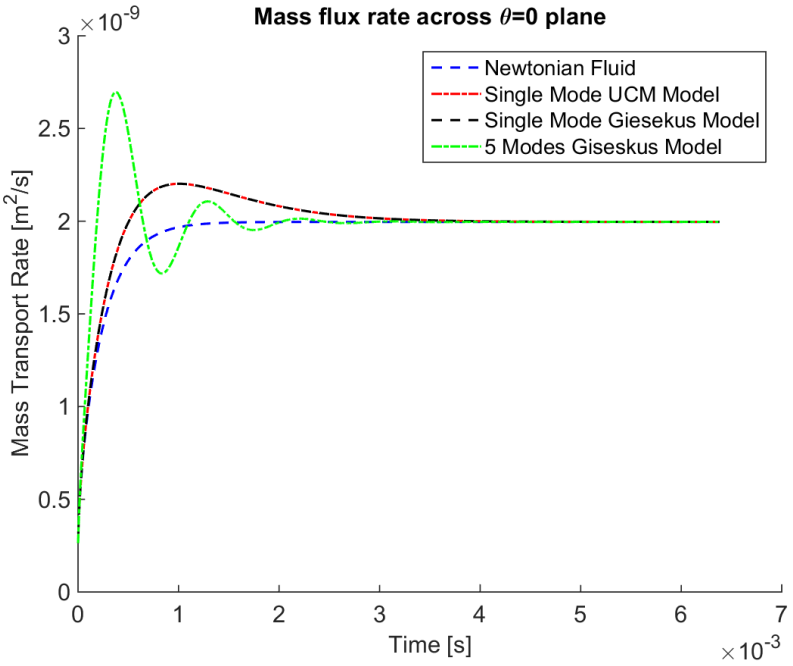

Figure 2.17: Mass transport flux rate across the $\theta = 0$ plane for the swirling flow with different types of fluids

creating a downward flow near the wall and upward flow at the center of the culture. The mass flux rate across the $\theta = 0$ plane is shown in Figure 2.19 for all four constitutive models (viscous, 1-mode UCM, 1-mode Giesekus, 5-mode Giesekus), with the result that after differences due to transients , they all converge to the same bulk flow rate for the pulsatile lower plate driving condition.

Next in Figure 2.20, we analyze the primary flow field, u_θ, in particular, the envelopes of u_θ across the gap, as well as the displacement time series at the edge of the cell culture at different heights. The resulting envelopes of the velocity exhibit a linear dependence across the gap. It can be shown that the shear strain and shear rate envelopes across the gap are also linear, corresponding to the so-called gap loading limit that is designed and exploited in rotational rheometers [26] [7]. We note that this gap loading behavior holds for this current set of parameters, and we return below to explore conditions that induce nonlinear primary flow behavior and departures from the gap-loading limit.

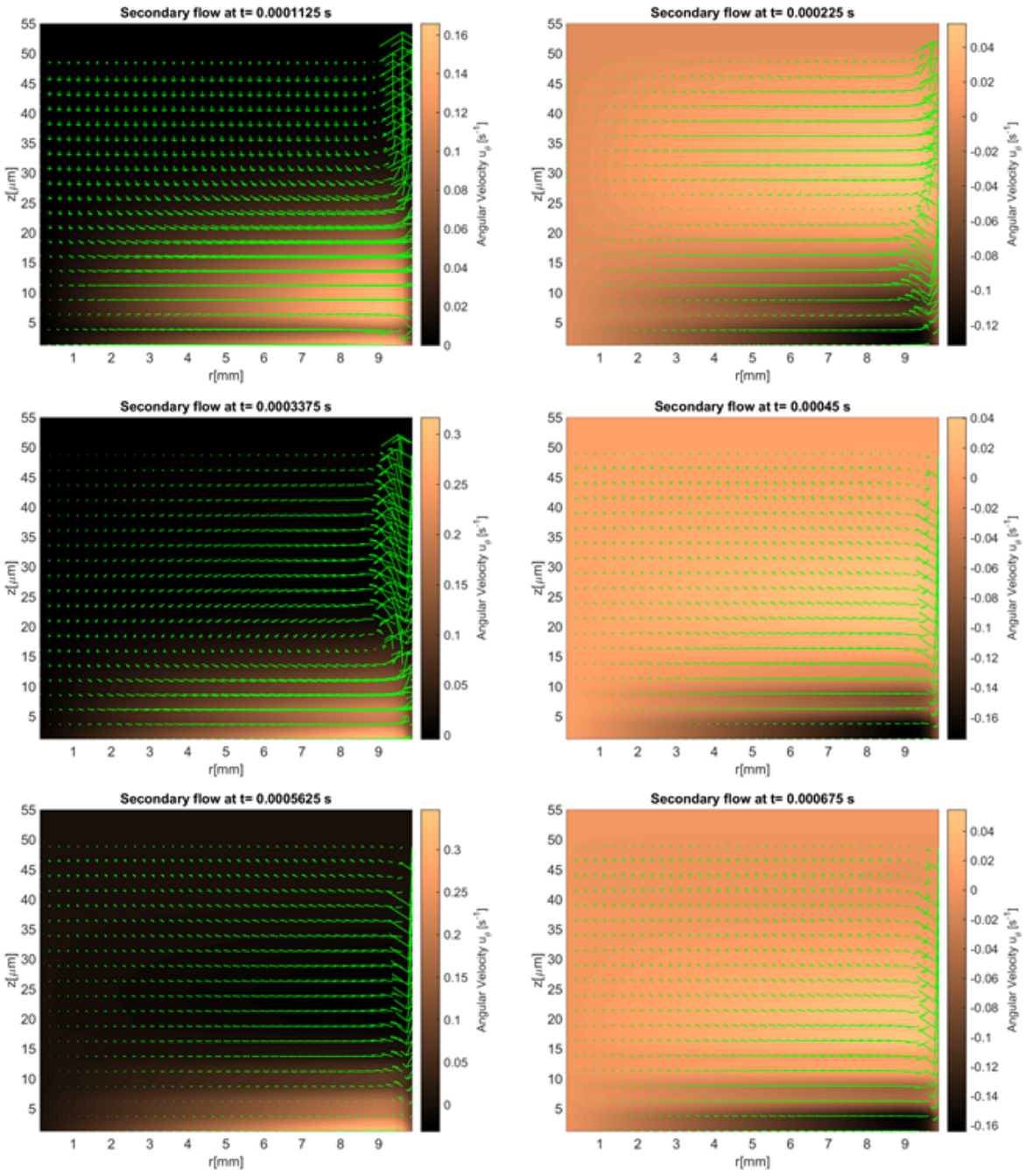

Figure 2.18: Flow field for a 5 modes Giesekus fluid with parameters specified in Table 2.3 with the oscillatory driving condition in Section 2.4; the velocity field in the plot is the secondary flow (u_r *vs* u_z)

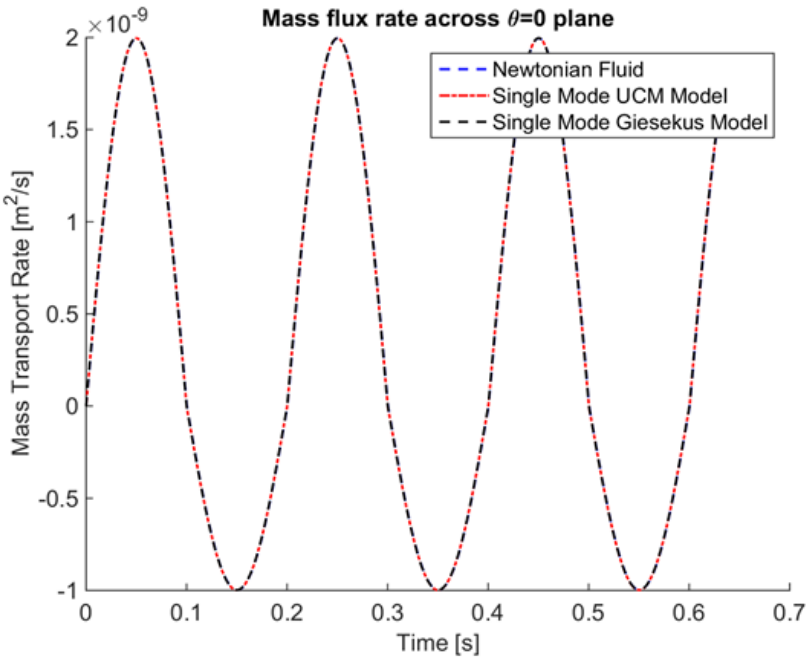

Figure 2.19: Mass transport flux rate across one $\theta = 0$ plane with oscillatory driving condition for 5 modes Giesekus fluid with parameters specified in Table 2.3;

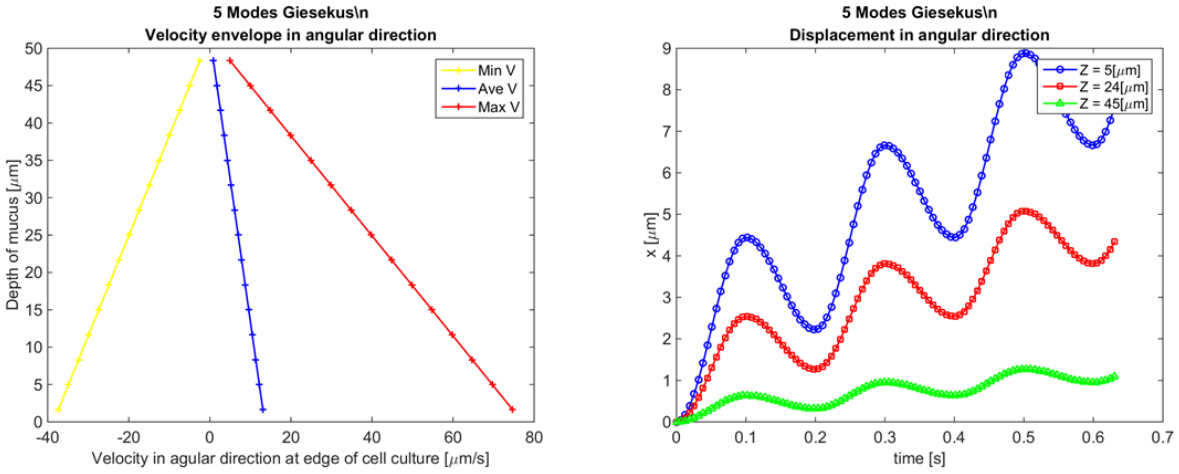

Figure 2.20: Left: Velocity envelopes in angular direction at the edge of cell culture; Right: displacement in angular direction at the edge of cell culture at different heights for 5 modes Giesekus fluid with parameters specified in Table 2.3;

2.7 Large Amplitude Oscillatory Shear(LAOS) Analysis of Nonlinearity

The linear primary flow profiles and shear strain and shear rate envelopes from the last section imply two things: the flow conditions fall within the gap-loading regime and the driving conditions induce a linear viscoelastic response, i.e., steady state results from Giesekus models overlap with those of the UCM model. However, to rigorously assess the linear or nonlinear regime for the given driving conditions, the standard procedure is to impose a sinusoidal shear strain at the bottom plate, rather than the angular velocity boundary condition of our simulations thus far. Then one checks for higher harmonic generation in the flow field [12] [4] [6]. The oscillatory driving condition at the bottom of the cell culture for u_θ does not imply a sinusoidal shear strain. Therefore, we calculate the driving condition for u_θ that is equivalent to an imposed sinusoidal shear strain.

$$imposed\ shear\ strain\ at\ bottom\ plate\ = \gamma_0 \sin(\omega t)$$

$$imposed\ shear\ rate = \gamma_0 \omega \cos(\omega t)$$

$$shear\ rate = \frac{1}{2}(\frac{\partial u_\theta}{\partial r} - \frac{u_\theta}{r})$$

$$u_\theta(r,z,t)\mid_{z=0} = C \cdot r + 2\gamma_0 \omega \cos(\omega t) \cdot r \cdot \log(r),\ C\ is\ a\ constant \tag{2.1}$$

where C is an arbitrary constant. With the above u_θ that results in a sinusoidal driving shear strain, we can apply the standard nonlinear (Fourier) viscoelastic metrics for large amplitude oscillatory shear [12].

We choose a set of parameters for the equation above such that the theta-component of the velocity resembles the conditions imposed in the previous section, as illustrated in Figure 2.21.

We calculate the Fourier decomposition of the resulting shear strain, shear rate and shear stress. We found that there are no higher harmonics greater than 3% of the fundamental harmonic. Furthermore, everywhere in the cell culture, the shear strain is a sine function and the shear rate is a cosine function. Figure 2.22 shows the envelopes of shear strain and shear stress across the height of the cell culture at radius r = 0.5R.

Figure 2.23 shows the normalized Lissajous curves at different locations of our cell culture. Lissajous curves offer a qualitative analysis of the stress waveforms [22]. Elastic Lissajous curves

show the oscillatory stress as a parametric function of the strain, whereas viscous Lissajous curves show the stress against the rate of strain. In this way, for an elastic solid, the elastic Lissajous curves are represented by straight lines and viscous Lissajous curves by circles, while the opposite is true for a viscous fluid. In the small amplitude regime for a generic viscoelastic fluid, both elastic and viscous Lissajous curves are ellipses. Any departure from a perfect ellipse signals that the nonlinear LAOS regime has been reached.

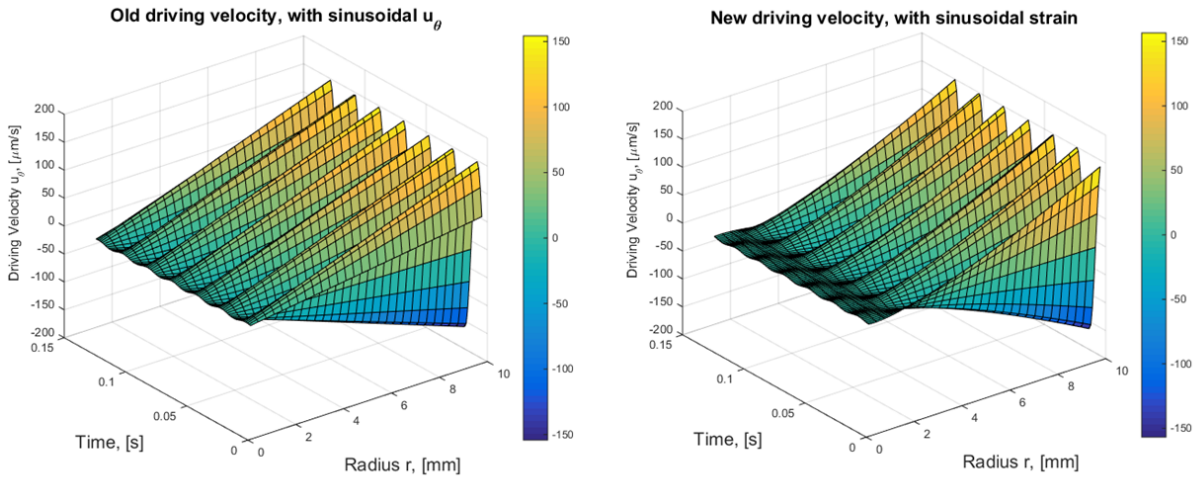

Figure 2.21: Left: Driving condition for u_θ where u_θ is a sinusoidal function of time; Right: Driving condition for u_θ where shear strain is a sinusoidal function of time

These results imply that, with the prescribed magnitude of the imposed angular velocity, the solution resides in the gap-loading and the linear regime of the viscoelastic model. Since we are in the linear regime, we can characterize the viscoelasticity of the mucus flow by calculating the linear storage modulus $G^{'}$, and loss modulus $G^{'}$, versus position in the culture [Figure 2.24].

Next, we explore the implications relative to linear and nonlinear flow when the mucus "hurricane" is localized in the middle of the cell culture and does not extend all the way to the culture wall. The effective radius of mucus flow is therefore smaller than the cell culture radius R=10mm. In the next simulation, we set the effective radius of the mucus flow as 5mm instead of 10mm and change the magnitude of the oscillatory driving velocity accordingly to match the experimental observation. Figure 2.25 shows the envelopes of shear strain and shear stress across the height of the cell culture at radius r = 0.5*R. They no longer scale linearly across the gap. Since the strain (and strain rate)

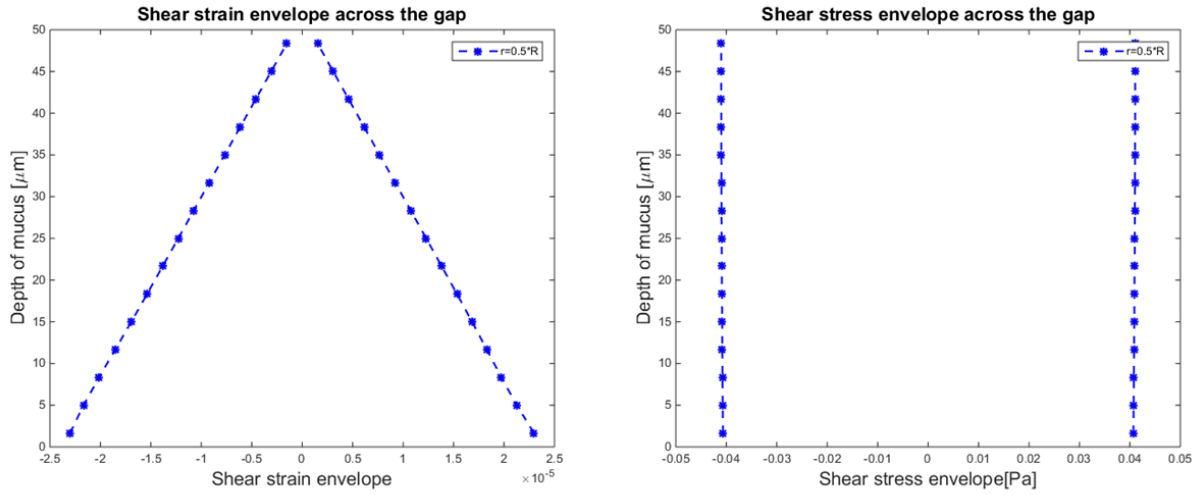

Figure 2.22: The envelopes of shear strain(left) and shear stress(right) across the gap at $r = 0.5 * R$

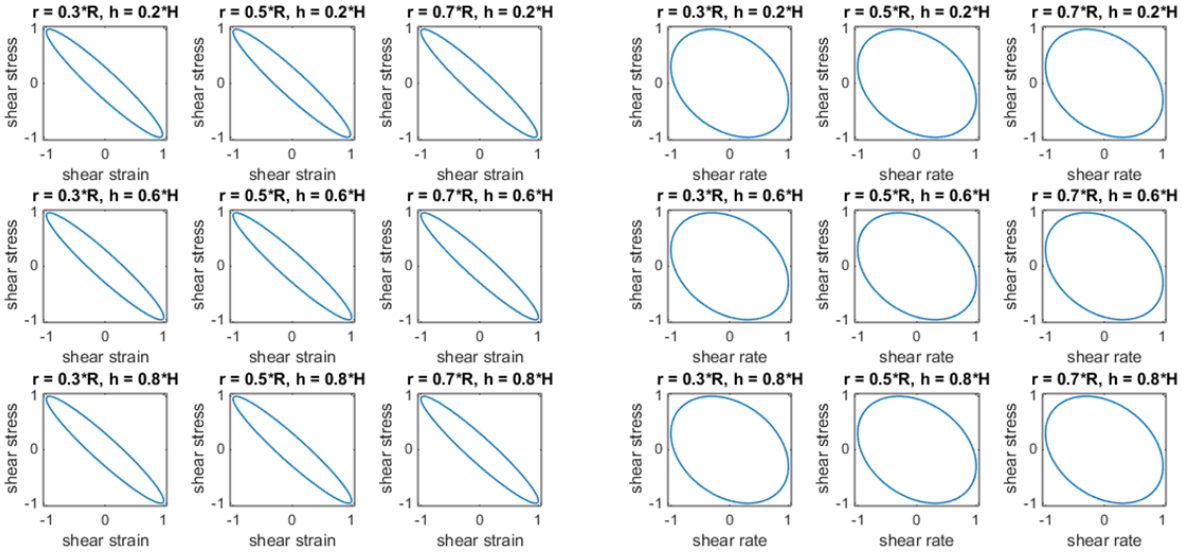

Figure 2.23: Normalized Lissajous curves of shear stress VS shear strain (left) and shear stress VS shear rate (right) at different positions of the cell culture

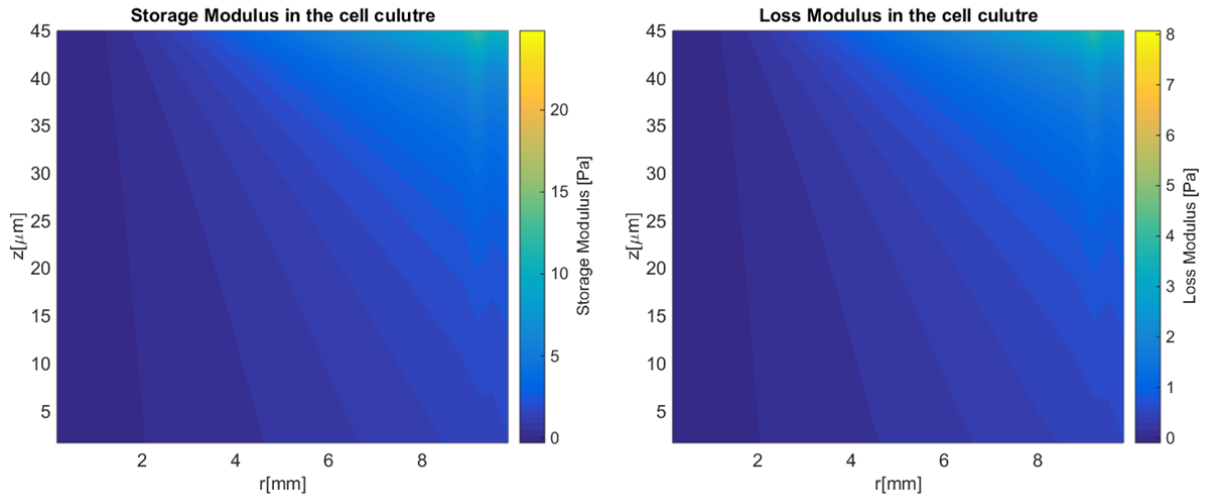

Figure 2.24: Storage Modulus $G^{'}$ (Left) and Loss Modulus $G^{''}$ (Right) everywhere in the cell culture

no longer scale linearly and the shear stress is not constant across the gap, Figure 2.26 indicates that for these conditions, the system is no longer in the gap-loading limit. The next step is to determine whether or not the model response is linear or nonlinear. Figure 2.26 shows LAOS analysis results at r=0.4*R and h=0.4*H, where the Lissajous curves now show a nonlinear response. These nonlinear response can be quantified by means of the stress decomposition [4] and Chebyshev expansion [6]. For oscillatory shear with an imposed sinusoidal strain, the resultant stress can be decomposed into elastic and viscous stresses by using symmetry arguments [4]. Ewoldt and McKinley suggested an orthogonal decomposition of the elastic and viscous stresses using Chebyshev polynomials [6]. The signs of third harmonic Chebyshev coefficients e_3 (elastic stress) and $_3$ (viscous stress) indicate the nature of the elastic and viscous nonlinearities. For our data $e_3 < 0$ and $_3 > 0$ implying the local mucus flow at this position in the culture is strain-softening and shear-thickening.

We now characterize nonlinearity of the mucus flow for reasonable ranges of cell culture parameters with the 5-mode Giesekus mucus model with parameters in Table 2.3. Figure 2.27 shows the linear and nonlinear regime for mucus flow with respect to the aspect ratio of the hurricane (radial extent versus mucus depth) and mean driving velocity u_θ at r=0.5*R. When the aspect ratio is less than 100 and the mean u_θ is greater than 70 $\mu m/s$, the mucus transport resides in the nonlinear regime . A similar characterization of nonlinear mucus response can be carried out versus constitutive characterization of mucus, which we omit.

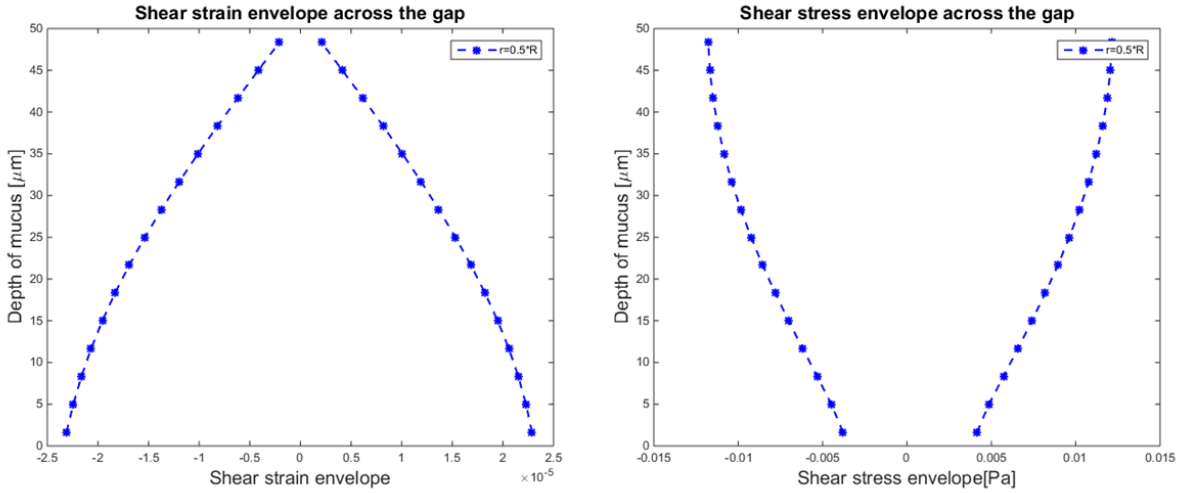

Figure 2.25: The envelopes of shear strain(left) and shear stress(right) across the gap at $r = 0.5 * R$ with $R = 5mm$.

2.8 Advection-diffusion of Drug Concentrations

In this section, we consider the scenario when an initial concentration of drug (or dye) is dropped at the surface of the mucus layer, which besides being transported by the underlying velocity field, it can diffuses freely in the HBE cell culture. We assume the drug does not alter the mucus properties or flow field and that there is no affinity between the mucus gel network and the diffusing particles. We further assume that the PCL-mucus interface absorbs any drug concentration that reaches it. Finally, we use the flow fields obtained from our previous results using the 5-mode Giesekus model from Table 1 and the cilia driving condition in Section 2.4.

For a drug concentration C with constant diffusion coefficient D, the transport of C inside the mucus flow can be describe by the following advection-diffusion equation

$$\frac{\partial C}{\partial t} = D\Delta(C) - \nabla \cdot (\boldsymbol{u}C) + \boldsymbol{S}$$

where $\boldsymbol{S}$ is the source of the concentration. Here we assume we have an initial concentration of C_0 and no extra source, i.e. $\boldsymbol{S} = 0$. In cylindrical form, the equation becomes

$$\frac{\partial C}{\partial t} = D[\frac{1}{r}\frac{\partial}{\partial r}(r\frac{\partial C}{\partial r}) + \frac{1}{r^2}\frac{\partial^2 C}{\partial \theta^2} + \frac{\partial^2 C}{\partial z^2}] - \frac{u_r}{r}\frac{\partial}{\partial r}(rC) - \frac{u_\theta}{r}\frac{\partial C}{\partial \theta} - u_z\frac{\partial C}{\partial z}$$

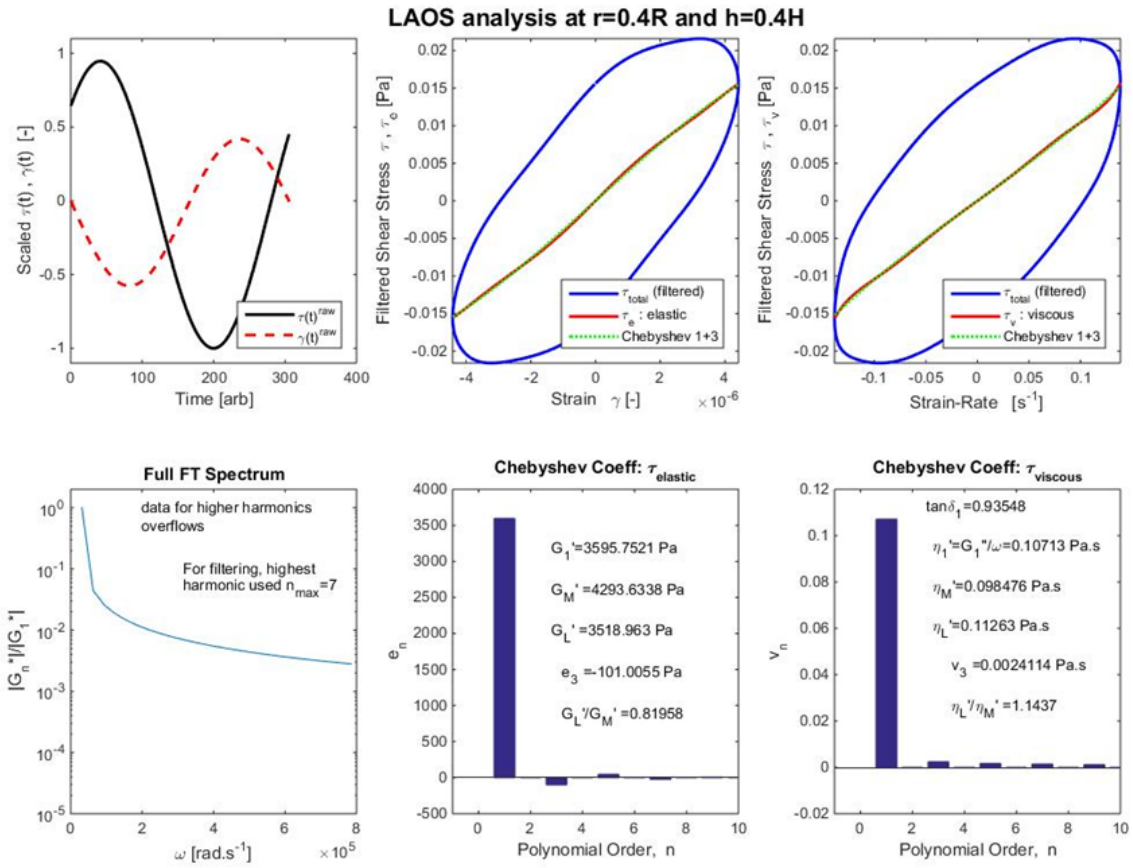

Figure 2.26: LAOS analysis for nonlinear viscoelasticity at $r = 0.4 * R$ and $h = 0.4 * H$ with $R = 5mm$.

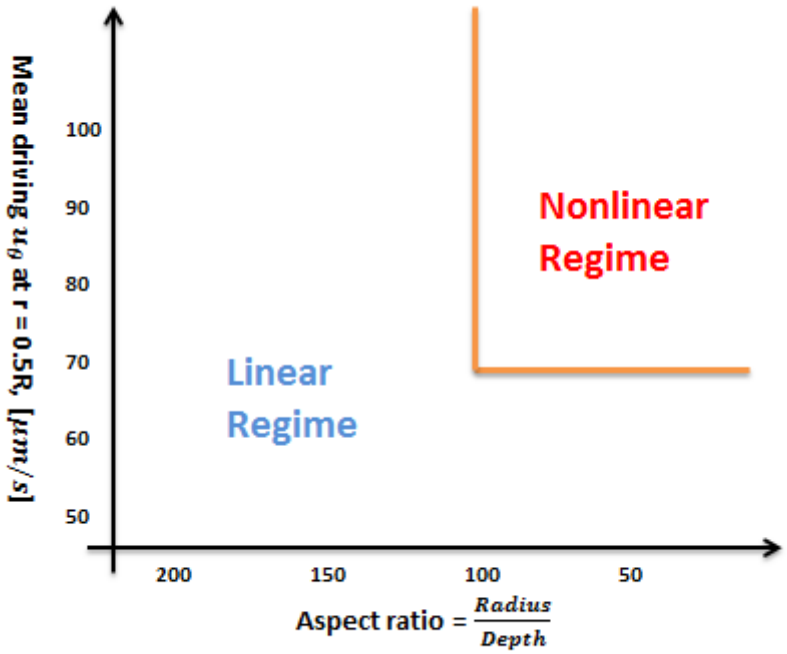

Figure 2.27: Characterizing the linear and nonlinear regime for mucus flow with respect to the aspect-ratio and mean driving u_θ at $r = 0.5 * R$

We assume axisymmetry of the flow, but depending on the symmetry of the initial concentration C_0, the advection-diffusion of C inside the cell culture might or might not be axisymmetric. However, if C_0 is axisymmetric, the concentration will remain so. In this case the advection-diffusion equation reduces to

$$\frac{\partial C}{\partial t} = D[\frac{1}{r}\frac{\partial}{\partial r}(r\frac{\partial C}{\partial r}) + \frac{\partial^2 C}{\partial z^2}] - \frac{u_r}{r}\frac{\partial}{\partial r}(rC) - u_z\frac{\partial C}{\partial z}$$

The boundary condition at the bottom plate is absorbing. The above equations are solved using a finite different method. The unsteady velocity field is extracted from the stationary results in Section 2.6.2.

Initially, a unit mass of drug is initially deposited in a small circular domain at the center of the surface of the cell culture, that is we set C_0 to be a disk of unit concentration with radius 0.1 mm at the center of the air-mucus interface. Figure 2.28 depicts the surface of the cell culture and the red dot is the domain of initial uniform concentration of the drug.

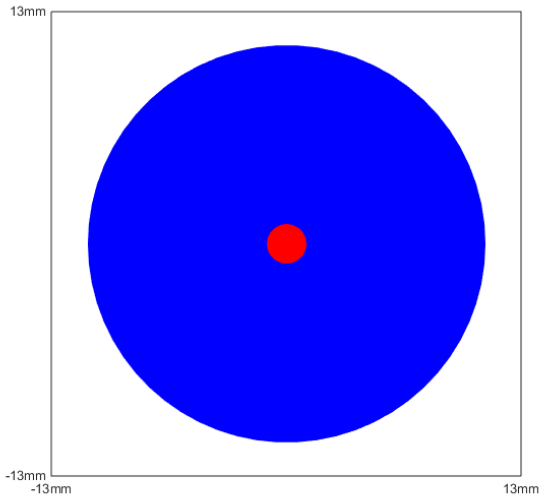

Figure 2.28: Initial drug concentration type 1; Blue disk shows the surface of the cell culture; red disk is the initial concentration of unit drug at the surface.

Using this initial condition, we investigate the effect of the diffusion coefficient on the distribution of drug concentration in space and time. The dimensionless Peclet number, Pe, describes the relation

of advection relative to diffusion,

$$Pe = \frac{advective\ transport\ rate}{diffusive\ transport\ rate} = \frac{L \cdot V}{D}$$

where L is the characteristic length, which is our case is $1 \times 10^{-2} m$ (length of the radius), V is the characteristic flow velocity, which is our case is $1 \times 10^{-9} m/s$ (mean local velocity in the r direction, note the mean local velocity in the θ direction is $1 \times 10^{-4} m/s$). The diffusion coefficient D that I used here ranges from 1×10^{-15},1×10^{-14},$\cdots$,1×10^{-8},1×10^{-7} m^2/s . Therefore the corresponding Pe are 1×10^{-4}, 1×10^{-3}, 1×10^{-2}, 1×10^{-1}, 1, 1×10^{2}, 1×10^{3}, 1×10^{4}.

Figure 2.29 and Figure 2.30 shows the advection-diffusion process for the drug concentration with $Pe = 0.1$ and $Pe = 10$ under the initial condition in Figure 2.28. Note that those figures are plotted in a reduced 2D rectangle because of the axisymmetric assumption, see Figure 2.6 for details. And as we can see from those plots, it seems like the drug is primarily diffusing in the z direction, but not in the r direction. This perception is incorrect. It only looks this way because of the large aspect-ratio we have for the HBE cell culture ($10mm$ length of radius and $50\mu m$ depth of mucus give us an aspect-ratio of 200). Therefore, with this large aspect-ratio and initial condition, most of the drug would be absorbed by the bottom plate long before it makes any significant transport in the radial direction.

Figure 2.31 shows the percentage of the drug concentration absorbed at the bottom plate by the exterior domain to the initial circle of drug concentration. When Pe is small (D is large), almost no drug will be absorbed on the outer part of the bottom plate . Since the drug primarily diffuses in the z direction because of the large aspect-ratio (10 mm radius, 50 μm depth, or aspect ratio of 200). Therefore, with this large aspect ratio and initial condition, most of the drug would be absorbed in a slightly larger radius domain at the bottom plate, with minimal radial diffusion and minimal influence of advection by the mucus flow. Even when $Pe = 1 \times 10^4$ ($D = 1 \times 10^{-15} m^2/s$), only 5.2% of the drug concentration is absorbed by the outer part" of the bottom plate. Hence the effect of mucus flow on the absorption of the drug concentration is minimal under these conditions. Figure 2.31 shows the time it takes for 95% of the drug concentration to be absorbed by the outer part of the bottom plate as a function of Pe.

If our purpose is for the drug to be absorbed "evenly" by the whole bottom plate of the cell

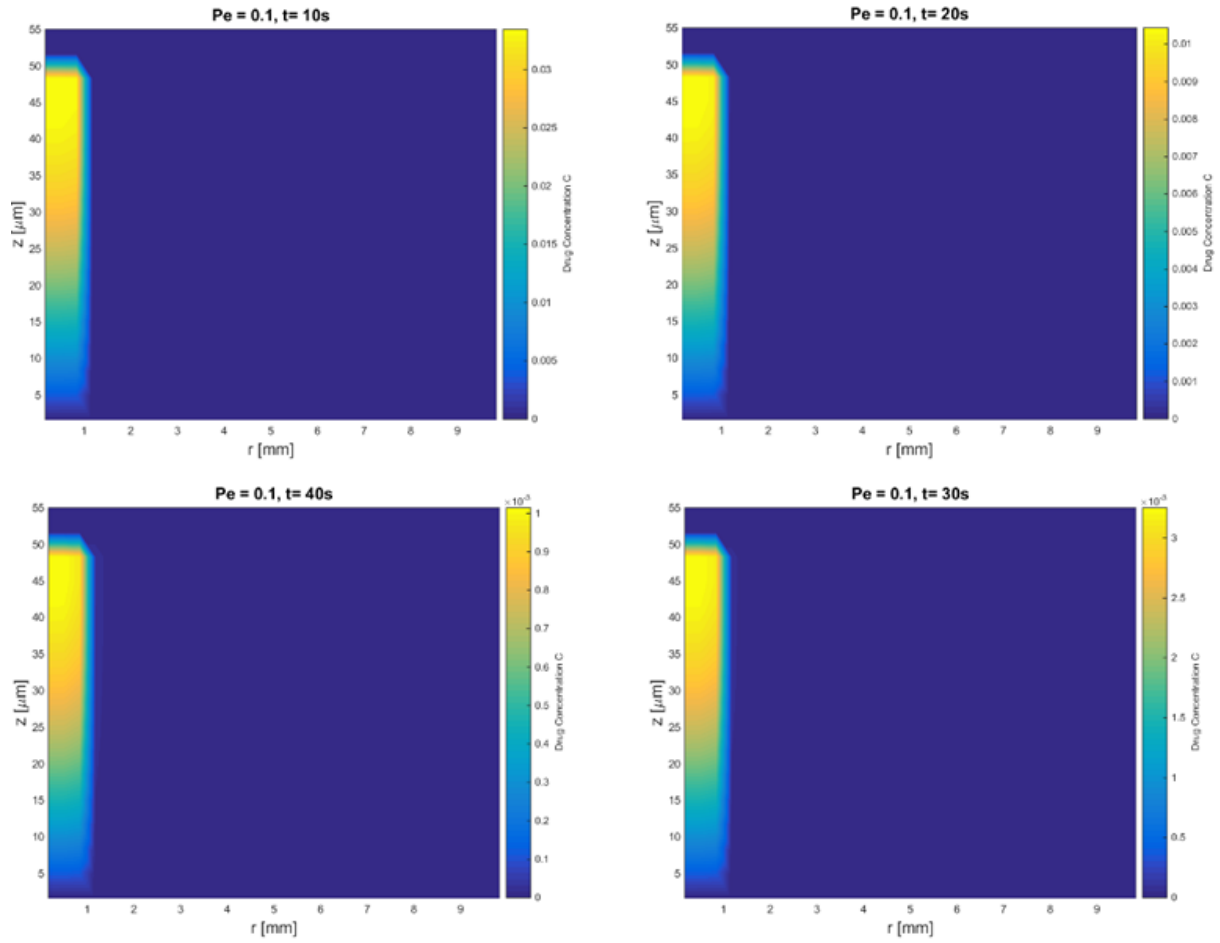

Figure 2.29: The advection-diffusion of the drug concentration with $Pe = 0.1$ in the mucus flow

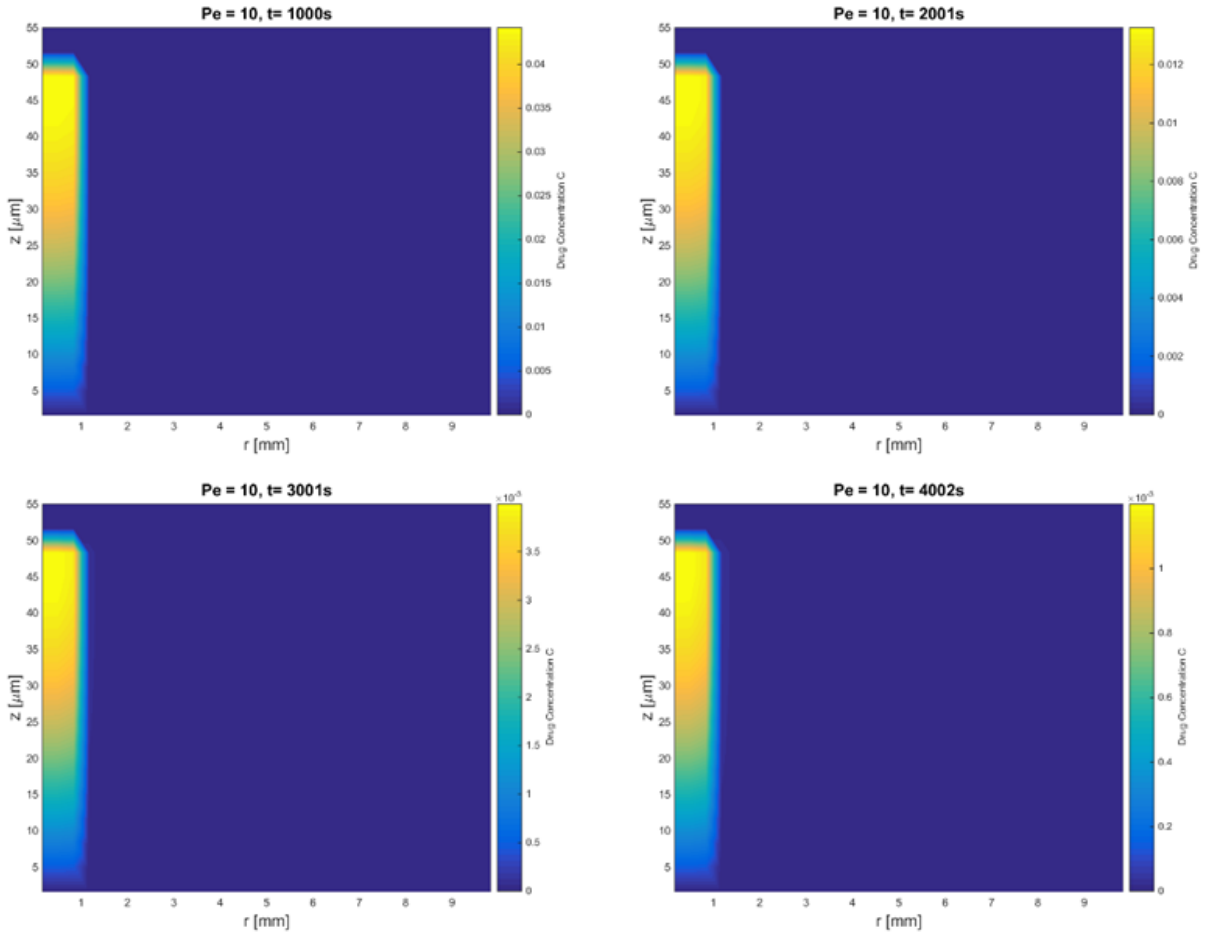

Figure 2.30: The advection-diffusion of the drug concentration with $Pe = 10$ in the mucus flow

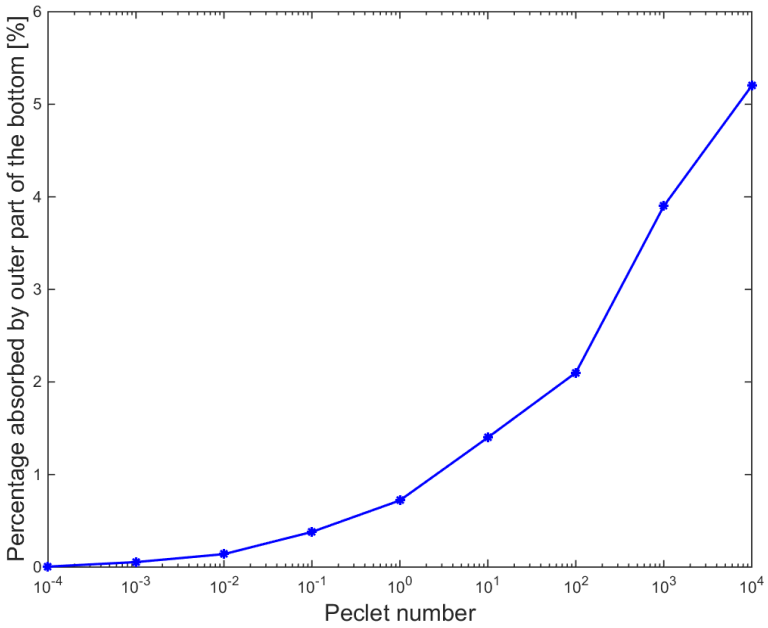

Figure 2.31: The percentages of the drug concentration absorbed by outer part" of the bottom plate in the end versus Peclet number Pe

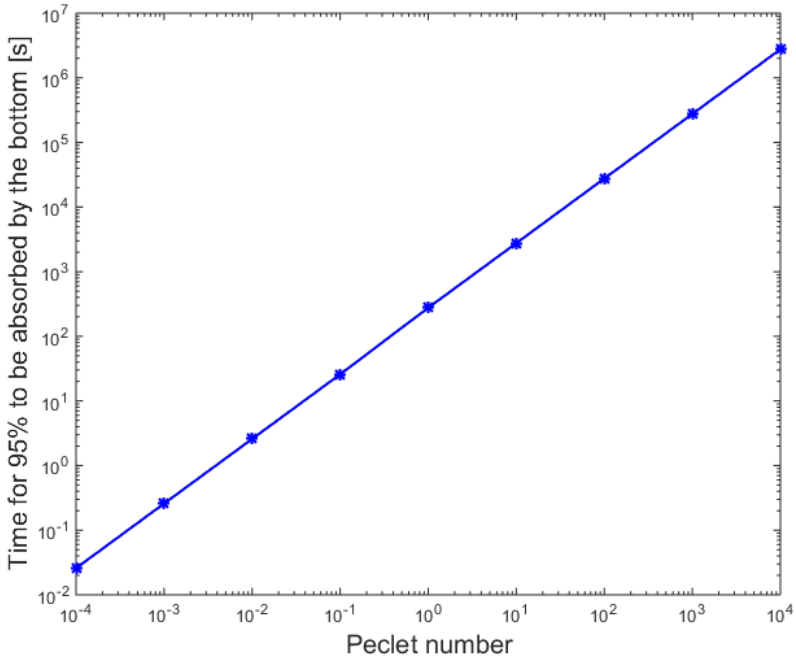

Figure 2.32: The time it takes for 95% of the drug concentration to be absorbed by the bottom of the cell culture versus Peclet number Pe

culture, the initial drop in Figure 2.28 would not result in our goal. We could instead initially spread the drug evenly on the entire surface of the mucus flow. Or more efficiently, we could take advantage of mucus "hurricane", and drop the drug along a radius with $\theta = 0$ of the surface of the mucus flow, see Figure 2.33.

Next we explore different domains of deposition of the drug at the air-mucus interface (Figure 2.33). To quantify absorption across the different initial conditions, we measure the percentage of the drug absorbed by a fan in the bottom plate with $-\frac{\pi}{12} < \theta < \frac{\pi}{12}$, as illustrated in Figure 2.34. This part takes up $\frac{1}{12}$ (or 8.33%) portion of the entire bottom disk and is in the opposite direction as the initial distribution of drug. If the drug is evenly absorbed by the bottom plate, this fan area would absorb 8.33% of the total drug concentration. The closer the percentage absorbed by this fan area is to 8.33%, the more effective the influence of advection. Figure 2.35 shows the result of the percentage of drug concentration absorbed by the fan area in the bottom plate versus Peclet number. We can see when $Pe < 0.1$, the drug transport is not effective; when $Pe > 1$, the drug transport is effective and when $Pe > 10^2$, the drug transport is extremely effective since the percentage is quite close to the "perfect" score of 8.33%.

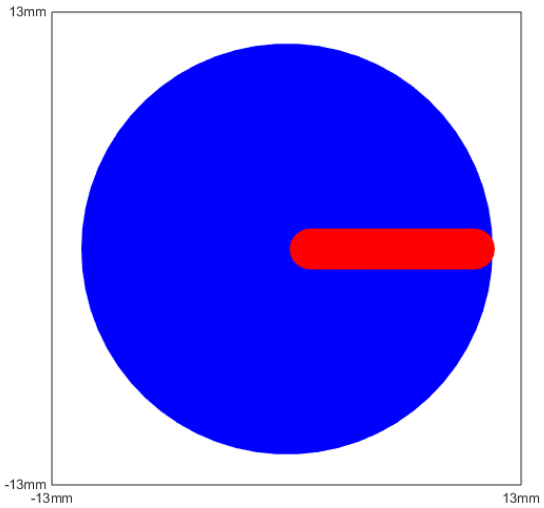

Figure 2.33: Initial drug concentration type 1; Blue disk shows the surface of the cell culture; red line is the initial concentration of unit drug at the surface.

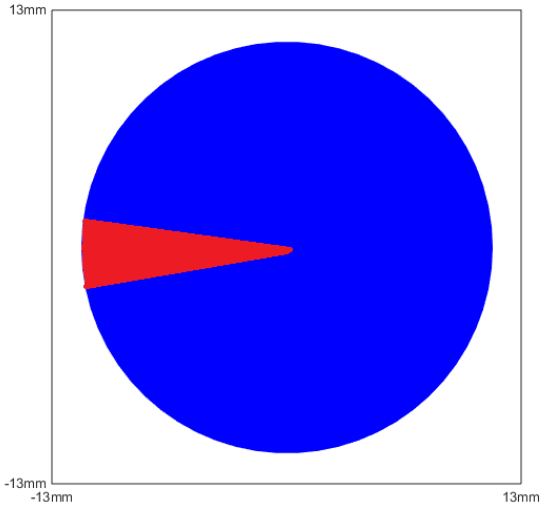

Figure 2.34: Initial drug concentration type 1; Blue disk shows the bottom of the cell culture; the red fan stands for the area where $-\frac{\pi}{12} < \theta < \frac{\pi}{12}$.

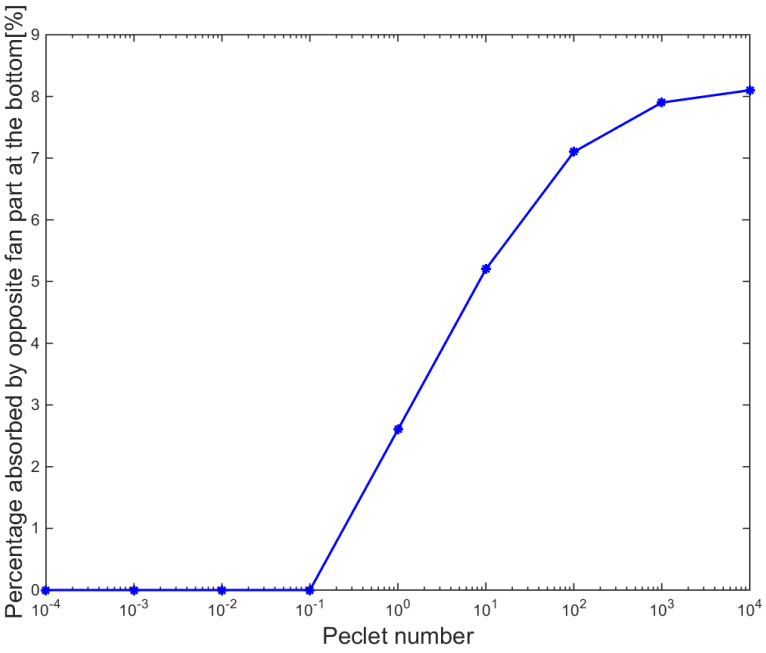

Figure 2.35: Percentage of drug concentration absorbed by the fan area in the bottom plate versus Peclet number Pe.

2.9 Validating the Numerical Methods

The numerical methods we use here are adopted from [24]. Marker and Cell (MAC) method [20] is used here to track the movement of the free surface. In the MAC method, artificial massless trackers are placed near the free surface and are transported according to the fluid velocity. Cells are flagged as fluid cells, surface cells and empty cells based on the location of all markers. Those markers are able to track the free surface movement. A second order finite difference method is used to discretized the space derivative on a staggered grid. Forward Euler scheme is used here for the time integration.

2.9.1 Convergence

In the following test, we use 4 different sizes of grids (30 by 30, 40 by 40, 50 by 50 and 60 by 60) to calculate the flow field and free surface shape of the swirling flow (constant angular driving velocity) of the same singe mode UCM fluid, with We=1.0. After the flow reaches quasi-steady state, we check the free surface shapes and the velocity field at the middle height of the cylinder to see whether the numerical results converges or not.

The following four figures [Figure 2.36 to 2.39] show the results. From [Figure 2.36 to 2.38] about the velocities components, it's easy to see that the code converges as the grid gets finer. And last figure [Figure 2.39] about the free surface suggests that the free surface curve also converges, but with a slower rate.

2.9.2 Benchmarking

Here we first compare the evolution of the tangential velocities [Figure 2.40] after the stop of the rotating disk with the result [Figure 14] from [27]. Then we compare the tangential velocity distribution for a single mode UCM fluid after stabilization [Figure 2.41], with the result [Figure 6] from [27]. By looking at Figure 2.40 and 2.41, we can see that the result for tangential velocity distribution from our numerical method matches the result from [27] [Figure 6 and 14]. This should suggest that our numerical algorithm is correct.

As we have seen in Section 2.6.1, one significant difference between viscoelastic fluid and Newtonian fluid in swirling flow is that viscoelastic fluid has the so called Quelleffekt [5]. The free

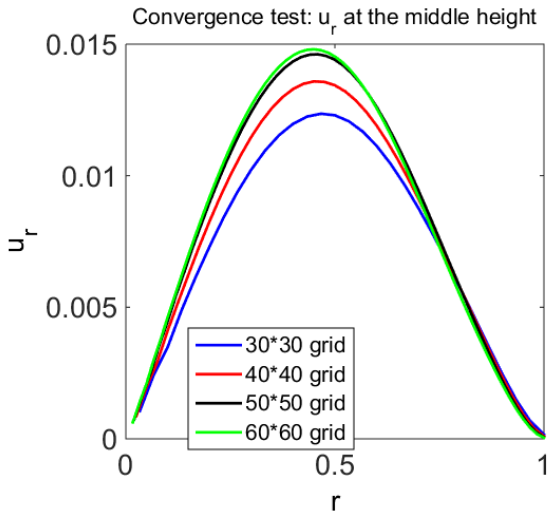

Figure 2.36: Convergence test: u_r at the middle height for a single UCM fluid

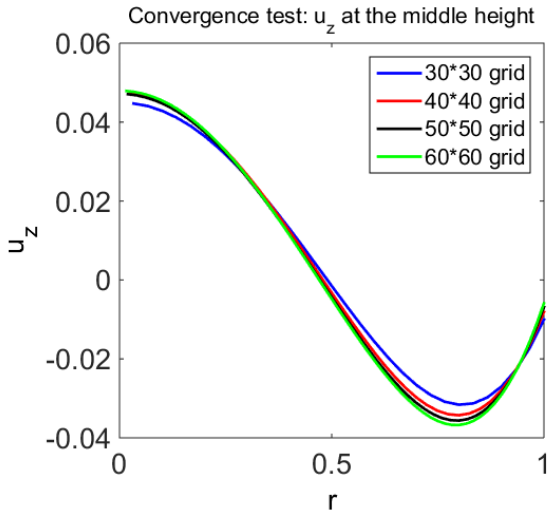

Figure 2.37: Convergence test: u_z at the middle height for a single UCM fluid

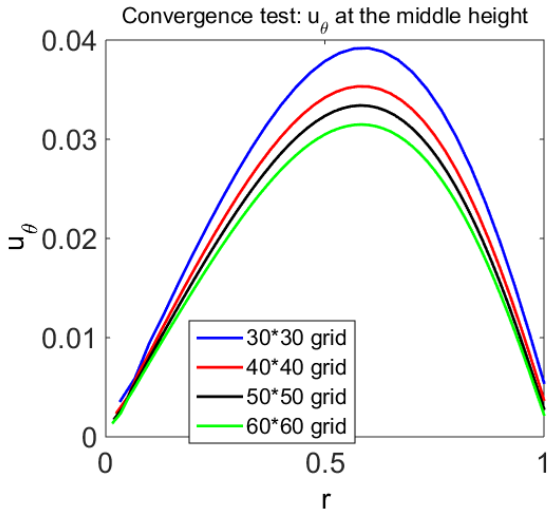

Figure 2.38: Convergence test: u_theta at the middle height for a single UCM fluid

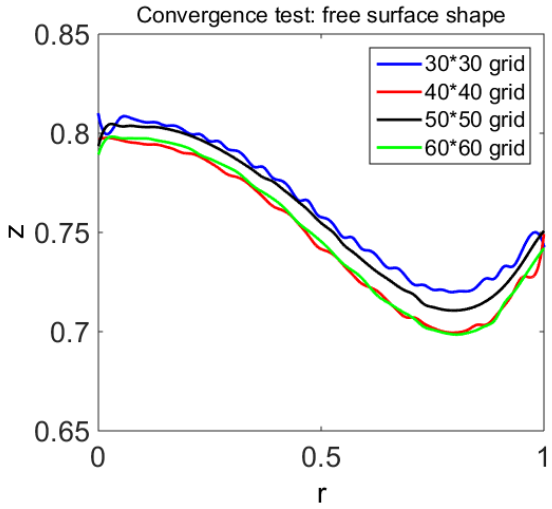

Figure 2.39: Convergence test: free surface shape for a single UCM fluid

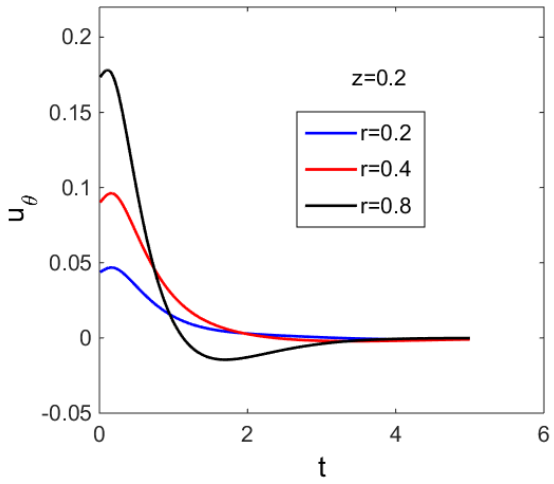

Figure 2.40: The evolution of the tangential velocities after the stop of the rotating disk for a single mode UCM fluid

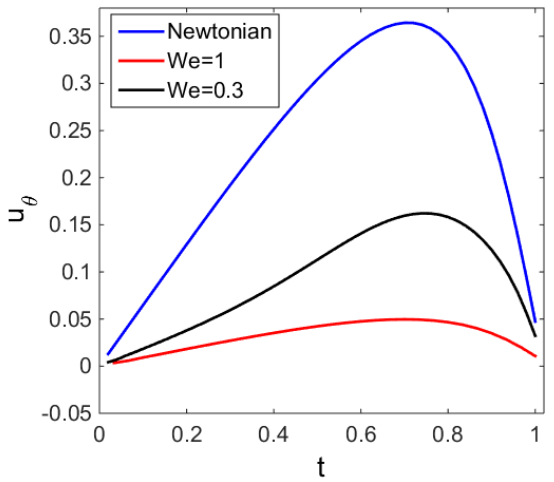

Figure 2.41: Tangential velocity distribution for a single mode UCM fluid after stabilization

surface of the viscoelastic fluid flows upwards along the axisymmetric swirling axis, rather than downwards as in the case of Newtonian fluid. Its like rod-climbing without a rod. And a bulge is generated at the upper surface of the fluid, which can be characterized by its vertical displacement along the axis of symmetry as illustrated in Figure2.42.

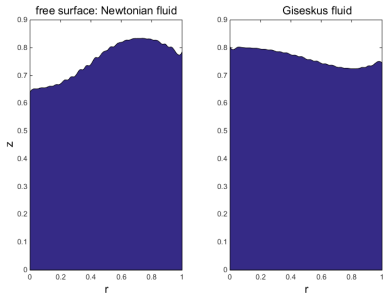

Figure 2.42: Illustration of Quelleffekt

In [5], Debbaut and Hocq studied the relationship between the displacement h (displacement in z-direction at the middle of the surface) and H (initial free surface height). In their numerical experiment they used Johnson-Segalman model to model a 2.5% aqueous polyacrylamide solution. Here I did the similar experiment with a single mode Giesekus fluid with $\alpha = 0.3$, and plot the same type of results that Debbaut and Hocq had for Johnson-Segalman model in [5]. Although exact match is not possible here, we focused on the trend and qualitative matching between our results and their results. In Figure 2.43 cited from [5], Debbaut and Hocq plot the free surface shape for various values of H and the displacement h of the upper surface along the axis of symmetry as a function of H for Johnson-Segalman model. In Figure 2.44 and 2.44, we plot the same figures but with our algorithm for a single mode Giesekus fluid. By comparing our results in Figure 2.44 and 2.45 and their results in Figure 2.43, both the shape of free surface and the relation between the displacement and initial surface height match with each other qualitatively. Given the fact that we used a different fluid model from theirs and the overall trends are the same, I believe this partially justifies our numerical code successfully captures the movement of the free surface.

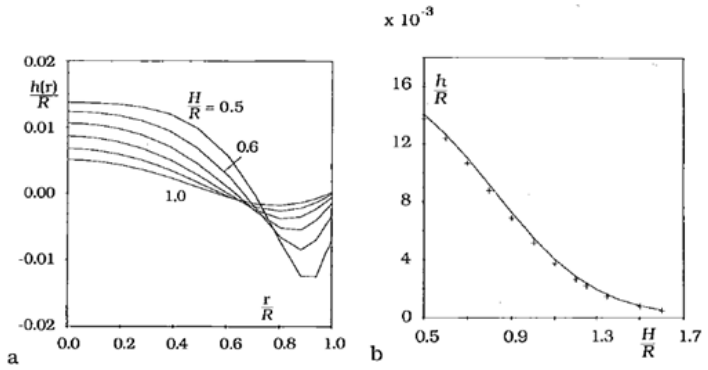

Figure 2.43: From [5]: free surface shapes for various H (a); Displacement h of the upper surface along the axis of symmetry as a function of H (b). Both for Johnson-Segalman model to model a 2.5% aqueous polyacrylamide solution.

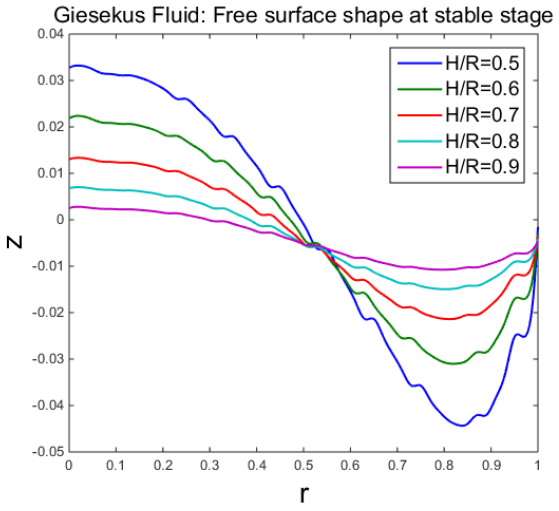

Figure 2.44: Displacement h of the upper surface along the axis of symmetry as a function of H for a single mode Giesekus fluid with $\alpha = 0.3$.

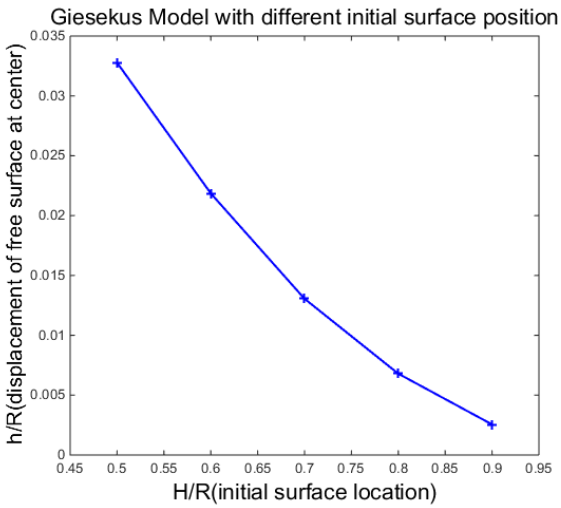

Figure 2.45: Free surface shapes for various H for a single mode Giesekus fluid with $\alpha = 0.3$.

CHAPTER 3

CONCLUSIONS

These are the first steps toward mucus flow in HBE cell culture simulations, with an idealized coarse-graining of the cilia forcing condition. First, we clearly show nonlinear viscoelasticity captures the simplest of observations: normal stress generation in shear leads to the peak of the free surface in the middle of the culture and a depression at the walls, and the corresponding flow profile is consistent with these free surface observations. Second, we characterized the linear and nonlinear viscoelastic regimes versus the radius and mean rotational velocity of the mucus "hurricane"; and designed viscoelastic metrics to study the property of mucus across the whole cell culture. Third, we examined the advection-diffusion process of a drug concentration dropped at the surface of the mucus flow against different drug diffusion coefficient. The absorption of the drug by the bottom plate of the cell cultures is explored for different initial concentrations and diffusion coefficient. And we illustrated the "flaw" of the absorption due to the large aspect-ratio and showed how to improve the effectiveness of the absorption. The future work includes the generalization of the code to 3D and extend the cilia forcing boundary conditions to experimentally measured metachronal wave patterns.

REFERENCES

[1] J. B. Bell, P. Colella, and H. M. Glaz. A second-order projection method for the incompressible navier-stokes equations. *Journal of Computational Physics*, 85(2):257–283, 1989.

[2] B. Button, L.-H. Cai, C. Ehre, M. Kesimer, D. B. Hill, J. K. Sheehan, R. C. Boucher, and M. Rubinstein. A periciliary brush promotes the lung health by separating the mucus layer from airway epithelia. *Science*, 337(6097):937–941, 2012.

[3] R. K. Chhetri, R. L. Blackmon, W.-C. Wu, D. B. Hill, B. Button, P. Casbas-Hernandez, M. A. Troester, J. B. Tracy, and A. L. Oldenburg. Probing biological nanotopology via diffusion of weakly constrained plasmonic nanorods with optical coherence tomography. *Proceedings of the National Academy of Sciences*, 111(41):E4289–E4297, 2014.

[4] K. S. Cho, K. Hyun, K. H. Ahn, and S. J. Lee. A geometrical interpretation of large amplitude oscillatory shear response. *Journal of Rheology (1978-present)*, 49(3):747–758, 2005.

[5] B. Debbaut and B. Hocq. On the numerical simulation of axisymmetric swirling flows of differential viscoelastic liquids: the rod climbing effect and the quelleffekt. *Journal of non-newtonian fluid mechanics*, 43(1):103–126, 1992.

[6] R. H. Ewoldt, A. Hosoi, and G. H. McKinley. New measures for characterizing nonlinear viscoelasticity in large amplitude oscillatory shear. *Journal of Rheology (1978-present)*, 52(6):1427–1458, 2008.

[7] J. D. Ferry. *Viscoelastic properties of polymers*. John Wiley & Sons, 1980.

[8] H. Giesekus. A simple constitutive equation for polymer fluids based on the concept of deformation-dependent tensorial mobility. *Journal of Non-Newtonian Fluid Mechanics*, 11(1):69–109, 1982.

[9] D. B. Hill and B. Button. Establishment of respiratory air–liquid interface cultures and their use in studying mucin production, secretion, and function. In *Mucins*, pages 245–258. Springer, 2012.

[10] D. B. Hill, V. Swaminathan, A. Estes, J. Cribb, E. T. O'Brien, C. W. Davis, and R. Superfine. Force generation and dynamics of individual cilia under external loading. *Biophysical journal*, 98(1):57–66, 2010.

[11] D. B. Hill, P. A. Vasquez, J. Mellnik, S. A. McKinley, A. Vose, F. Mu, A. G. Henderson, S. H. Donaldson, N. E. Alexis, R. C. Boucher, et al. A biophysical basis for mucus solids concentration as a candidate biomarker for airways disease. *PloS one*, 9(2):e87681, 2014.

[12] K. Hyun, M. Wilhelm, C. O. Klein, K. S. Cho, J. G. Nam, K. H. Ahn, S. J. Lee, R. H. Ewoldt, and G. H. McKinley. A review of nonlinear oscillatory shear tests: Analysis and application of large amplitude oscillatory shear (laos). *Progress in Polymer Science*, 36(12):1697–1753, 2011.

[13] V. Im Hof, P. Gehr, V. Gerber, M. Lee, and S. Schürch. In vivo determination of surface tension in the horse trachea and in vitro model studies. *Respiration physiology*, 109(1):81–93, 1997.

[14] M. Kesimer, S. Kirkham, R. J. Pickles, A. G. Henderson, N. E. Alexis, G. DeMaria, D. Knight, D. J. Thornton, and J. K. Sheehan. Tracheobronchial air-liquid interface cell culture: a model for innate mucosal defense of the upper airways? *American Journal of Physiology-Lung Cellular and Molecular Physiology*, 296(1):L92–L100, 2009.

[15] R. G. Larson. *The structure and rheology of complex fluids*, volume 33. Oxford university press New York, 1999.

[16] J. F. Lechner, A. Haugen, I. A. McClendon, and E. W. Pettis. Clonal growth of normal adult human bronchial epithelial cells in a serum-free medium. *In vitro*, 18(7):633–642, 1982.

[17] A. E. Likhtman and R. S. Graham. Simple constitutive equation for linear polymer melts derived from molecular theory: Rolie–poly equation. *Journal of Non-Newtonian Fluid Mechanics*, 114(1):1–12, 2003.

[18] C. W. Macosko and R. G. Larson. Rheology: principles, measurements, and applications. 1994.

[19] H. Matsui, S. H. Randell, S. W. Peretti, C. W. Davis, and R. C. Boucher. Coordinated clearance of periciliary liquid and mucus from airway surfaces. *Journal of Clinical Investigation*, 102(6):1125, 1998.

[20] S. McKee, M. Tomé, V. Ferreira, J. Cuminato, A. Castelo, F. Sousa, and N. Mangiavacchi. The mac method. *Computers & Fluids*, 37(8):907–930, 2008.

[21] A. L. Oldenburg, R. K. Chhetri, D. B. Hill, and B. Button. Monitoring airway mucus flow and ciliary activity with optical coherence tomography. *Biomedical optics express*, 3(9):1978–1992, 2012.

[22] W. Philippoff. Vibrational measurements with large amplitudes. *Transactions of The Society of Rheology (1957-1977)*, 10(1):317–334, 1966.

[23] M. Sanderson and M. Sleigh. Ciliary activity of cultured rabbit tracheal epithelium: beat pattern and metachrony. *Journal of Cell Science*, 47(1):331–347, 1981.

[24] M. Tomé, A. Castelo, J. Murakami, J. Cuminato, R. Minghim, M. Oliveira, N. Mangiavacchi, and S. McKee. Numerical simulation of axisymmetric free surface flows. *Journal of Computational Physics*, 157(2):441–472, 2000.

[25] P. A. Vasquez and M. G. Forest. Complex fluids and soft structures in the human body. In *Complex Fluids in Biological Systems*, pages 53–110. Springer, 2015.

[26] P. A. Vasquez, Y. Jin, K. Vuong, D. B. Hill, and M. G. Forest. A new twist on stokes second problem: Partial penetration of nonlinearity in sheared viscoelastic layers. *Journal of Non-Newtonian Fluid Mechanics*, 196:36–50, 2013.

[27] B. Yu, J. Wei, and Y. Kawaguchi. Swirling flow of a viscoelastic fluid with free surfacepart ii: Numerical analysis with extended marker-and-cell method. *Journal of fluids engineering*, 128(1):77–87, 2006.